A novel positive/negative projection in energy norm for the damage modeling of quasi-brittle solids

Jian-Ying Wu[a,*], Miguel Cervera[b]

[a]*State Key Laboratory of Subtropical Buildig Science, South China University of Technology, 510641 Guangzhou, China.*
[b]*CIMNE, Technical University of Catalonia, Edificio C1, Campus Norte, Jordi Girona 1-3, 08034 Barcelona, Spain.*

Abstract

The asymmetric tensile/compressive material behavior and microcracks closure-reopening (MCR) effects exhibited by quasi-brittle solids are of significant importance to the nonlinear responses of engineering structures under cyclic loading, e.g., earthquake excitations. Based on our previous work (Cervera et al., 1995; Faria et al., 1998; Wu et al., 2006) this work addresses a novel thermodynamically consistent unilateral damage model for concrete. In particular, the positive/negative projection (PNP) of the effective stress tensor and the additive bi-scalar damage constitutive relation are maintained owing to the conceptual simplicity and computational efficiency. It is found that the classical PNP widely adopted in the literature is not optimal for this damage model, since the resulting stiffness is not always of major symmetry. Consequently, a well-defined free energy potential does not exist in general cases and the model cannot be cast into the framework of thermodynamics with internal variables. Furthermore, the damage induced anisotropy cannot be captured, exhibiting excessive lateral deformations under uniaxial tension. To overcome the above issues, a novel PNP, variationally interpreted as the closest point projection of the effective stress in energy norm, is proposed with closed-form solution. With the novel PNP, the secant stiffness tensor of the proposed unilateral damage model always possesses major symmetry and exhibits orthotropic behavior under uniaxial tension and mixed tension/compression. The corresponding thermodynamics framework is then given, resulting in an energy release rate based rounded-Rankine type damage criterion appropriate for tensile failure in quasi-brittle solids. Several numerical examples of single-point verifications and benchmark tests are presented. It is demonstrated that the proposed model is capable of characterizing localized failure of concrete under proportional and non-proportional static loading, as well as the MCR effects under seismic cyclic loading.

Keywords:

Damage; thermodynamics; quasi-brittle failure; concrete; cyclic loading; microcracks closure-reopening; unilateral effects.

*Tel.: (+86) 20-87112787
Email address:* `jywu@scut.edu.cn` (Jian-Ying Wu)

1. Introduction

Failure of quasi-brittle solids, e.g., concrete, rock, ceramics, etc., is mainly dominated by microcracks evolution on the mesoscopic scale. On the one hand, they are prone to localized failure in dominant tension, and exhibit rather inferior tensile behavior and stiffness degradation compared to the relatively high strength and ductile performances in compression. On the other hand, microcracks tend to close upon load reversal such that the material stiffness can be largely recovered (Reinhardt and Cornelissen, 1984; Mazars et al., 1990), known as the so-called unilateral effects. The asymmetric tensile/compressive material behavior and microcracks closure-reopening (MCR) effects are of significant importance to the responses and safety of engineering structures under static and seismic loadings.

Owing to the pioneering work of Kachanov (1958), continuum damage mechanics (CDM) has nowadays been widely adopted in the constitutive modeling of concrete like quasi-brittle solids; see the monographs (Krajcinovic, 2003; Lemaitre and Desmorat, 2005; Murakami, 2012) and the references therein. Restricting our attention to concrete under cyclic loading, a large volume of damage models have been proposed in the literature; see Mazars and Pijaudier-Cabot (1989); Cervera et al. (1995); Faria et al. (1998); Li and Fenves (1998); Comi and Perego (2001); Wu et al. (2006); Abu Al-Rub and Kim (2010); Miehe et al. (2010a); Grassl et al. (2013) among many others. In most of these damage models, two scalar internal variables, say, i.e., d^+ and d^-, both in the range [0, 1], are adopted to characterize the asymmetric tensile/compressive material behavior, respectively. With this strategy, the MCR effects upon load reversals can also be modeled straightforwardly by (partially) activating/deactivating the corresponding damage variable dependent on the specific stress/strain state.

To the above end, it is necessary to discriminate the dominant tension (positive) and compression (negative) states in general 3-D cases. In the 1980s the French scholars first decomposed the stress tensor into its positive and negative components based on the spectral decomposition; see Mazars and Pijaudier-Cabot (1989) for the review. During this stage, another celebrated work is Ortiz (1985) in which the fourth-order positive/negative projection (PNP) operators of the stress tensors were first introduced explicitly in the damage constitutive relation. Since then, in the damage modeling of concrete the PNP of a specific second-order tensor, e.g., the strain (Simó and Ju, 1987; Ju, 1989), the nominal stress (Yazdani and Schreyer, 1990; Hansen and Schreyer, 1994, 1995; Lubarda et al., 1994) and the effective stress (Cervera et al., 1995; Faria et al., 1998; Wu et al., 2006; Abu Al-Rub and Kim, 2010; Grassl et al., 2013), etc., has been the standard strategy. Besides the expressions given in Ortiz (1985), two alternative fourth-order PNP operators were also proposed (Simó and Ju, 1987; Carol and Willam, 1996). In the last reference (Carol and Willam, 1996), different PNP operators for the damage modeling of the MCR effects were systematically investigated. It was found that for a generic anisotropic damage model, all the existing PNP operators cannot guaranteed zero energy dissipation during a closed loading cycle, violating the second law of thermodynamics. Recently, this issue was revisited by the author (Wu and Xu, 2013). Unified expressions for the classical fourth-order PNP operators were established with all the previous ones included as its particular examples. Furthermore, the thermodynamical consistent PNP operators were derived for the first time, completely removing the aforesaid issue.

Among the large quantities of damage models for concrete, the one proposed by Cervera et al. (1995) and Faria et al. (1998) deserves further comments. In this model the PNP of the effective stress was first adopted for modeling the asymmetric tensile/compressive material behavior and the MCR effects of concrete. This strategy results in a theoretically simple additive bi-scalar damage constitutive relation. In particular, the plastic strains can be straightforwardly incorporated by the effective stress space plasticity (Ju, 1989) as in the work of Wu et al. (2006). Furthermore, as the effective stress tensor is defined in the context of strain equivalence (Simó and Ju, 1987), the strain-driven numerical algorithm (Faria et al., 1998; Wu et al., 2006) is very robust and efficient, particularly useful for the application to practical engineering structures (Wu and Li, 2007). Owing to the theoretical and numerical advantages, the additive bi-scalar damage constitutive relation has been widely adopted in later development of concrete models (Li and Ren, 2009; Abu Al-Rub and Kim, 2010; Pelà et al., 2011; Gernay et al., 2013; Grassl et al., 2013). However, for the classical PNP scheme considered in the literature, this additive bi-scalar damage model degenerates in the uniaxial stress state to an isotropic one which is known being unable to capture the damage induced anisotropy. More importantly, the corresponding stiffness tensor is not of major symmetry in the mixed tension/compression states. That is, it is impossible to define a *unique* free energy potential function. Accordingly, the original additive bi-scalar damage model cannot be cast into the framework of thermodynamics with internal variables. This is in strong contrast to the bi-scalar damage models based on the positive/negative split of the stress or strain tensor (Mazars and Pijaudier-Cabot, 1989; Ortiz, 1985; Miehe et al., 2010a) which are thermodynamically consistent. Last but not the lest, another side effect is that the damage criteria can only be postulated in an *ad hoc* or heuristically manner.

In order to remedy the aforesaid issues, Cervera and Tesei (2017) recently proposed a *multiplicative* bi-scalar damage model which is distinct from the original additive one. The postulate of energy equivalence (Cordebois and Sidoroff, 1982; Carol et al., 2001) is employed to restore the major symmetry of the stiffness tensor. The classical PNP is performed on the strain tensor rather than the effective stress for the sake of numerical efficiency.

In this work, an alternative approach is proposed, in which the conceptual simplicity and numerical efficiency associated with the original additive bi-scalar damage model is preserved as much as possible. As we will show, the positive/negative components of a specific second-order tensor and the corresponding fourth-order PNP operators are not unique, unless an extra constraint is applied. Different supplementary condition yields rather distinct positive/negative components. In particular, the classical PNP scheme considered in the literature is only introduced in a heuristic manner for convenience. Therefore, it is possible to construct a novel PNP scheme such that the stiffness tensor of the original additive bi-scalar damage constitutive relation is always of major symmetry. Motivated by this viewpoint, the objective of this paper is four-fold: *(i)* to revisit the classical PNP scheme and to demonstrate its adverse effects on the damage model; *(ii)* to derive a novel variationally consistent PNP in energy norm and to give the explicit solution; *(iii)* to cast the additive bi-scalar damage model into the thermodynamics with internal variables; and finally, *(iv)* to illustrate its numerical performances in the modeling of concrete under static and seismic loadings.

The remainder of this paper is outlined as follows. Section 2 presents the original additive bi-scalar damage model. A generalized definition of the PNP is given with respect to the effective stress tensor. Section 3 addresses the classical

PNP scheme and its variational interpretation. The adverse effects on the original additive bi-scalar damage model are then demonstrated. On the one hand, these theoretical analyses consolidate the classical PNP scheme heuristically considered in the literature. On the other hand, they also shed lights to other alternative PNP schemes. Section 4 is devoted to the novel variationally consistent PNP scheme in energy norm and the explicit solutions. In Section 5 the original additive bi-scalar damage constitutive relation is re-derived within the thermodynamics with internal variables. In particular, an energy release rate based damage criterion appropriate for tensile failure in concrete like quasi-brittle solids is established with no *ad hoc* assumption. The novel additive bi-scalar damage model is then validated in Section 6 with numerical examples of single-point verification as well as benchmark tests of concrete under both static and seismic loadings. The most relevant concluding remarks are drawn in Section 7, followed by three appendices closing this paper.

Notation. Compact tensor notation is used as much as possible. As a general rule, scalar a is denoted by a light-face italic minuscule (Latin or Greek) letter; vector $\boldsymbol{a}$, second-order tensor $\boldsymbol{A}$ and fourth-order tensor $\mathbb{A}$ are signified by boldface minuscule, majuscule and boldface majuscule letters, respectively. Operators 'tr$(\cdot)$' and '$(\cdot)^{\text{sym}}$' indicate the trace and sum-type symmetrized operators, respectively, defined as $\text{tr}A = A_{ii}$ and $(A^{\text{sym}})_{ij} = (A_{ij} + A_{ji})/2$. Symbols '$\cdot$' and '$:$' denote the inner products with single and double contractions, respectively. The dyadic product '$\otimes$' and the symmetrized outer product '$\overline{\otimes}$' are defined as

$$(\boldsymbol{A} \otimes \boldsymbol{B})_{ijkl} = A_{ij}B_{kl}, \qquad (\boldsymbol{A} \,\overline{\otimes}\, \boldsymbol{B})_{ijkl} = \frac{1}{2}\big(A_{ik}B_{jl} + A_{il}B_{jk}\big)$$

Letters $\boldsymbol{1}$ and $\mathbb{I} := \boldsymbol{1} \,\overline{\otimes}\, \boldsymbol{1}$ signify the second-order and symmetric fourth-order identity tensors, respectively. The McAuley brackets $\langle x \rangle$ and Heaviside function $H(x)$ are defined as $\langle x \rangle = x$, $H(x) = 1$ if $x > 0$, and $\langle x \rangle = 0$, $H(x) = 0$ otherwise.

2. An effective stress based bi-scalar damage theory

In this section, the effective stress based additive bi-scalar damage theory proposed by the authors (Cervera et al., 1995; Faria et al., 1998; Wu et al., 2006) is presented, focusing on the PNP for modeling the asymmetric tensile/compressive material behavior and the MCR effects exhibited by quasi-brittle solids under cyclic loading.

2.1. Effective stress

In the absence of plastic strains, the effective stress tensor $\bar{\boldsymbol{\sigma}}$ in damaging solids is assumed to follow an isotropic linear elastic behavior. In accordance with the postulate of strain equivalence (Simó and Ju, 1987), it is defined as

$$\bar{\boldsymbol{\sigma}} = \mathbb{E}_0 : \boldsymbol{\epsilon}, \qquad \boldsymbol{\epsilon} = \mathbb{C}_0 : \bar{\boldsymbol{\sigma}} \tag{2.1}$$

for the fourth-order elasticity tensor $\mathbb{E}_0$ and compliance $\mathbb{C}_0$

$$\mathbb{E}_0 = 2G_0\big(\mathbb{I} + \hat{v}_0 \boldsymbol{I} \otimes \boldsymbol{I}\big), \qquad \mathbb{C}_0 = \frac{1}{E_0}\Big[(1 + v_0)\mathbb{I} - v_0 \boldsymbol{I} \otimes \boldsymbol{I}\Big] \tag{2.2}$$

4

where the shear modulus $G_0 := \frac{1}{2} E_0/(1 + v_0)$ is expressed in terms of Young's modulus E_0 and Poisson's ratio v_0; the modified Poisson's ratio $\hat{v}_0$ is defined as $\hat{v}_0 = v_0/(1 - 2v_0)$ in general 3-D and plane strain cases, and $\hat{v}_0 = v_0/(1 - v_0)$ for plane stress condition. Note that in the cases of plane strain and plane stress, the second-order identity tensor $\boldsymbol{I}$ and the fourth-order one $\mathbb{I}$ are the 2-D counterparts of their 3-D quantities.

2.2. Positive/negative projection (PNP)

In modeling the MCR effects under cyclic loading, one needs to characterize the distinct material behavior under dominant tension and compression, respectively. To this end, a specific state variable in the set $\mathscr{C}$ containing all second-order symmetric tensors, e.g., the strain $\boldsymbol{\epsilon}$, nominal stress $\boldsymbol{\sigma}$, effective stress $\bar{\boldsymbol{\sigma}}$, etc., is decomposed into its positive (tensile) and negative (compressive) components (Ortiz, 1985; Simó and Ju, 1987; Mazars and Pijaudier-Cabot, 1989; Cervera et al., 1995). As the plastic strains can be incorporated straightforwardly (Ju, 1989; Wu et al., 2006), in this work the effective stress tensor $\bar{\boldsymbol{\sigma}} \in \mathscr{C}$ is adopted and spectrally decomposed as

$$\bar{\boldsymbol{\sigma}} = \sum_n \bar{\sigma}_n \boldsymbol{P}_{nn} = \bar{\boldsymbol{\sigma}}^+ + \bar{\boldsymbol{\sigma}}^-, \qquad \bar{\sigma}_n = \boldsymbol{P}_{nn} : \bar{\boldsymbol{\sigma}} \qquad (2.3)$$

where $\bar{\sigma}_n$ and $\boldsymbol{p}_n$ represent the n-th ($n = 1, 2, 3$) principal value of the effective stress tensor $\bar{\boldsymbol{\sigma}}$ and the corresponding principal vector, respectively, with the later defining the second-order symmetric tensor $\boldsymbol{P}_{nn} := \boldsymbol{p}_n \otimes \boldsymbol{p}_n$. Note that the subscript n does not refer to the dummy index of a tensor (or vector), but rather, it represents the quantity associated with the n-th principal value.

In the decomposition (2.3), the positive/negative components $\bar{\boldsymbol{\sigma}}^{\pm}$ are coaxial to the parent effective stress tensor $\bar{\boldsymbol{\sigma}}$. Without loss of generality, they are expressed as

$$\bar{\boldsymbol{\sigma}}^+ = \sum_n \bar{\sigma}_n^+ \boldsymbol{P}_{nn}, \qquad \bar{\boldsymbol{\sigma}}^- = \bar{\boldsymbol{\sigma}} - \bar{\boldsymbol{\sigma}}^+ = \sum_n \bar{\sigma}_n^- \boldsymbol{P}_{nn} \qquad (2.4)$$

where $\bar{\sigma}_n^+ \geq 0$ and $\bar{\sigma}_n^- := \bar{\sigma}_n - \bar{\sigma}_n^+ \leq 0$ are the principal values of the positive effective stress tensor $\bar{\boldsymbol{\sigma}}^+ \in \mathscr{C}^+$ and the negative one $\bar{\boldsymbol{\sigma}}^- \in \mathscr{C}^-$, respectively, such that

$$\bar{\sigma}_n^{\pm} = \boldsymbol{P}_{nn}^{\pm} : \bar{\boldsymbol{\sigma}}, \qquad \boldsymbol{P}_{nn}^+ + \boldsymbol{P}_{nn}^- = \boldsymbol{P}_{nn} \qquad (2.5)$$

The second-order symmetric tensors $\boldsymbol{P}_{nn}^{\pm}$, to be determined later, depend on the adopted PNP scheme. The sets $\mathscr{C}^+$ and $\mathscr{C}^-$ collect all the positive and negative semi-definite second-order symmetric tensors, respectively. Note that the closed convex sets $\mathscr{C}^{\pm} \subset \mathscr{C}$ are both cones in the sense that $\boldsymbol{\Sigma} \in \mathscr{C}^{\pm}$ imply $k \boldsymbol{\Sigma} \in \mathscr{C}^{\pm} \ \forall k \geq 0$ (Del Piero, 1989).

With the relations (2.5), the positive/negative effective stress tensors (2.4) can be rewritten as

$$\bar{\boldsymbol{\sigma}}^{\pm} = \mathbb{P}^{\pm} : \bar{\boldsymbol{\sigma}}, \qquad \mathbb{P}^+ + \mathbb{P}^- = \mathbb{I} \qquad (2.6)$$

for the fourth-order projection operators $\mathbb{P}^{\pm}$

$$\mathbb{P}^+ = \sum_n \boldsymbol{P}_{nn} \otimes \boldsymbol{P}_{nn}^+, \qquad \mathbb{P}^- = \mathbb{I} - \mathbb{P}^+ \qquad (2.7)$$

both of which possess the minor symmetry but not necessarily the major one.

The positive/negative effective stress tensors $\bar{\boldsymbol{\sigma}}^{\pm}$ and the associated PNP operators $\mathbb{P}^{\pm}$ have not been *uniquely* defined yet and several alternatives exist. This fact makes it possible to investigate different PNP schemes and select the one optimal for the presented additive bi-scalar damage theory.

Remark 2.1 Note that the projection operators satisfy the idempotent property (Meyer, 2000), i.e.,

$$\mathbb{P}^{\pm} : \mathbb{P}^{\pm} : \bar{\boldsymbol{\sigma}} = \mathbb{P}^{\pm} : \bar{\boldsymbol{\sigma}}^{\pm} = \bar{\boldsymbol{\sigma}}^{\pm} \qquad \Longrightarrow \qquad \mathbb{P}^{+} : \bar{\boldsymbol{\sigma}}^{-} = \mathbb{P}^{-} : \bar{\boldsymbol{\sigma}}^{+} = \boldsymbol{0} \tag{2.8}$$

That is, the positive/negative decomposition is an orthogonal projection. □

2.3. Additive bi-scalar damage constitutive relation

Corresponding with the positive/negative components $(\bar{\boldsymbol{\sigma}}^{+}, \bar{\boldsymbol{\sigma}}^{-})$ of the effective stress tensor $\bar{\boldsymbol{\sigma}}$, two damage variables $d^{+} \in [0, 1]$ and $d^{-} \in [0, 1]$ are introduced to characterize the material behavior under tension/compression, respectively.

In line with our previous work (Cervera et al., 1995; Faria et al., 1998; Wu et al., 2006), the following damage constitutive relation is considered

$$\boldsymbol{\sigma} = (1 - d^{+})\bar{\boldsymbol{\sigma}}^{+} + (1 - d^{-})\bar{\boldsymbol{\sigma}}^{-} = \mathbb{E} : \boldsymbol{\epsilon} \tag{2.9a}$$

for the secant stiffness tensor $\mathbb{E}$

$$\mathbb{E} = \left[(1 - d^{+})\mathbb{P}^{+} + (1 - d^{-})\mathbb{P}^{-} \right] : \mathbb{E}_0 = (\mathbb{I} - \mathbb{D}) : \mathbb{E}_0 \tag{2.9b}$$

where the fourth-order damage tensor $\mathbb{D} = d^{+}\mathbb{P}^{+} + d^{-}\mathbb{P}^{-}$ is not necessarily isotropic.

On the one hand, as the positive/negative effective stress tensors $\bar{\boldsymbol{\sigma}}^{\pm}$ are both coaxial to $\bar{\boldsymbol{\sigma}}$, the stress tensor (2.9a) can be spectrally decomposed as

$$\boldsymbol{\sigma} = \sum_{n} \sigma_n \boldsymbol{P}_{nn}, \qquad \sigma_n = (1 - d^{+})\bar{\sigma}_n^{+} + (1 - d^{-})\bar{\sigma}_n^{-} \tag{2.10}$$

for the principal stresses σ_n. That is, the stress tensor $\boldsymbol{\sigma}$ is also coaxial to the effective counterpart $\bar{\boldsymbol{\sigma}}$ such that all calculations can be performed in the principal space (of the effective stress tensor or of the strain tensor).

On the other hand, as the coefficients $(1 - d^{\pm}) \in [0, 1]$ change neither the principal vectors nor the signs of principal values, the stress tensor (2.9a) or (2.10) admits a similar PNP, i.e.,

$$\boldsymbol{\sigma} = \boldsymbol{\sigma}^{+} + \boldsymbol{\sigma}^{-}, \qquad \boldsymbol{\sigma}^{\pm} = (1 - d^{\pm})\bar{\boldsymbol{\sigma}}^{\pm} \tag{2.11}$$

Calling for the orthogonality condition (2.8)$_2$, the positive/negative components $\boldsymbol{\sigma}^{\pm} \in \mathscr{C}^{\pm}$ are expressed as

$$\boldsymbol{\sigma}^{\pm} = \mathbb{P}^{\pm} : \left[(1 - d^{+})\bar{\boldsymbol{\sigma}}^{+} + (1 - d^{-})\bar{\boldsymbol{\sigma}}^{-} \right] = \mathbb{P}^{\pm} : \boldsymbol{\sigma} \tag{2.12}$$

In other words, the projection operators $\mathbb{P}^{\pm}$ of the effective stress tensor $\bar{\sigma}$ also extract the corresponding positive/negative components $\sigma^{\pm}$ of the stress tensor σ.

Accordingly, the additive bi-scalar constitutive relations (2.9) can be rewritten inversely as

$$\epsilon = \mathbb{C} : \sigma = \mathbb{C}_0 : \bar{\sigma}, \qquad \mathbb{C} := \mathbb{E}^{-1} = \mathbb{C}_0 : \left(\frac{1}{1 - d^+} \mathbb{P}^+ + \frac{1}{1 - d^-} \mathbb{P}^- \right) \tag{2.13a}$$

or, equivalently,

$$\epsilon = \frac{1}{(1 - d^+) E_0} \Big[(1 + \nu_0) \sigma^+ - \nu_0 \, \text{tr}(\sigma^+) I \Big] + \frac{1}{(1 - d^-) E_0} \Big[(1 + \nu_0) \sigma^- - \nu_0 \, \text{tr}(\sigma^-) I \Big] \tag{2.13b}$$

Note the difference between this model and the Mazars and Pijaudier-Cabot (1989) one; see Remark 2.2.

The above additive bi-scalar damage constitutive relations are established based on the postulate of strain equivalence (Simó and Ju, 1987). The resulting secant stiffness tensor (2.9b) and compliance tensor (2.13a)$_2$ depend explicitly on the expressions of the PNP operators. As will be shown later, for the classical PNP widely adopted in the literature (Ortiz, 1985; Simó and Ju, 1987; Carol and Willam, 1996; Wu and Xu, 2013), the secant stiffness tensor and compliance in general do not possess major symmetry, resulting in non-existence of a well-defined free energy potential. Consequently, the constitutive relation (2.9) or (2.13) cannot be cast into the framework of thermodynamics with internal variables. This issue is to be tackled in this work by introducing a novel PNP in energy norm.

Remark 2.2 Mazars and Pijaudier-Cabot (1989) proposed a celebrated stress-based bi-scalar damage model for concrete under cyclic loading. In this model, the positive/negative projection of the stress tensor σ is employed and the constitutive relation is given by

$$\epsilon = \frac{1}{(1 - d^+) E_0} \Big[(1 + \nu_0) \sigma^+ - \nu_0 \, \langle \text{tr} \sigma \rangle I \Big] + \frac{1}{(1 - d^-) E_0} \Big[(1 + \nu_0) \sigma^- + \nu_0 \, \langle -\text{tr} \sigma \rangle I \Big] = \mathbb{C} : \sigma \tag{2.14a}$$

where the secant compliance $\mathbb{C}$ is expressed as

$$\mathbb{C} = \frac{1}{(1 - d^+) E_0} \Big[(1 + \nu_0) \mathbb{P}^+ - \nu_0 \, H(I_1) I \otimes I \Big] + \frac{1}{(1 - d^-) E_0} \Big[(1 + \nu_0) \mathbb{P}^- + \nu_0 \, H(-I_1) I \otimes I \Big] \tag{2.14b}$$

for the first invariant $I_1 = \text{tr} \sigma$ of the stress tensor σ. Note that the trace operator $\text{tr}(\cdot)$ is acted to the total stress σ rather than to the positive/negative components $\sigma^{\pm}$ as in Eq. (2.13b). A similar bi-scalar damage model was proposed in Miehe et al. (2010a) employing the PNP of the strain tensor. □

2.4. Damage evolution laws

The above additive bi-scalar damage theory is completed with the evolution laws for the damage variables $d^{\pm}$. Though other alternatives exist, let us consider the following effective stress based damage criteria (Simó and Ju, 1987; Ju, 1989)

$$g^{\pm}(Y^{\pm}, r^{\pm}) = Y^{\pm}(\bar{\sigma}) - r^{\pm} \leq 0, \qquad r^{\pm} = \max_{t \in [0, T]} \left(r_0^{\pm}, Y_t^{\pm} \right) \tag{2.15}$$

such that the following Kuhn-Tucker loading/unloading conditions hold

$$\dot{d}^{\pm} \geq 0, \qquad g^{\pm}(Y^{\pm}, r^{\pm}) \leq 0, \qquad \dot{d}\,g^{\pm}(Y^{\pm}, r^{\pm}) \equiv 0 \tag{2.16}$$

where the damage driving forces $Y^{\pm}(\bar{\sigma})$ are expressed in terms of the effective stress $\bar{\sigma}$; the damage thresholds $r^{\pm}$, with the initial values $r_0^{\pm}$, denote the maximum driving forces ever reached.

Accordingly, the damage variables $d^{\pm}$ can be postulated as non-decreasing functions of the driving forces $r^{\pm}$, i.e.,

$$d^{\pm} = \hat{d}^{\pm}(r^{\pm}) \qquad \Longrightarrow \qquad \dot{d}^{\pm} = h^{\pm}\dot{r}^{\pm} \tag{2.17}$$

for the damage hardening functions $h^{\pm} := \partial\hat{d}^{\pm}/\partial r^{\pm} \geq 0$.

The explicit expressions for the damage variables $\hat{d}^{\pm}(r^{\pm})$ are determined by fitting those experimental test data under uniaxial tension/compression; see Section 6 for an example.

2.5. Constitutive relation in rate form and material tangent

In order to derive the damage constitutive relation in rate form, it is necessary to calculate the rates $\dot{\bar{\sigma}}^{\pm}$ of the positive/negative effective stress tensors $\bar{\sigma}^{\pm}$. After some mathematic manipulations (Faria et al., 2000; Wu et al., 2006; Wu and Xu, 2013), it follows that

$$\dot{\bar{\sigma}}^{+} = \mathbb{Q}^{+} : \dot{\bar{\sigma}}, \qquad \dot{\bar{\sigma}}^{-} = \dot{\bar{\sigma}} - \dot{\bar{\sigma}}^{+} = \mathbb{Q}^{-} : \dot{\bar{\sigma}} \tag{2.18}$$

where the fourth-order tensors $\mathbb{Q}^{\pm} := \partial\bar{\sigma}^{\pm}/\partial\bar{\sigma}$ is expressed as

$$\mathbb{Q}^{+} = \mathbb{P}^{+} + 2\sum_{n}\sum_{m>n}\frac{\bar{\sigma}_n^{+} - \bar{\sigma}_m^{+}}{\bar{\sigma}_n - \bar{\sigma}_m}\boldsymbol{P}_{nm}\otimes\boldsymbol{P}_{nm}, \qquad \mathbb{Q}^{-} = \mathbb{I} - \mathbb{Q}^{+} \tag{2.19}$$

for the second-order symmetric tensor $\boldsymbol{P}_{nm} = \left(\boldsymbol{p}_n\otimes\boldsymbol{p}_m\right)^{\mathrm{sym}}$. Owing to the orthogonal property $\boldsymbol{P}_{nm} : \bar{\sigma} = 0$ for $m \neq n$ (Wu and Xu, 2013), the following identities hold

$$\mathbb{Q}^{\pm} : \bar{\sigma} = \mathbb{P}^{\pm} : \bar{\sigma} = \bar{\sigma}^{\pm}, \qquad \dot{\mathbb{Q}}^{\pm} : \bar{\sigma} = \dot{\bar{\sigma}}^{\pm} - \mathbb{Q}^{\pm} : \dot{\bar{\sigma}} = \boldsymbol{0} \tag{2.20}$$

That is, the fourth-order tensors $\mathbb{Q}^{\pm}$ extract the same positive/negative components $\bar{\sigma}^{\pm}$ as the *irreducible* PNP operators $\mathbb{P}^{\pm}$ do.

Taking derivative of the stress (2.9a) to time yields

$$\dot{\sigma} = \left(1 - d^{+}\right)\dot{\bar{\sigma}}^{+} + \left(1 - d^{-}\right)\dot{\bar{\sigma}}^{-} - \bar{\sigma}^{+}\dot{d}^{+} - \bar{\sigma}^{-}\dot{d}^{-} = \left(\mathbb{I} - \mathbb{Q} - \mathbb{H}\right) : \dot{\bar{\sigma}} \tag{2.21}$$

where the fourth-order tensors $\mathbb{Q}$ and $\mathbb{H}$ are expressed as

$$\mathbb{Q} = d^{+}\mathbb{Q}^{+} + d^{-}\mathbb{Q}^{-}, \qquad \mathbb{H} = h^{+}\bar{\sigma}^{+}\otimes\boldsymbol{\Lambda}^{+} + h^{-}\bar{\sigma}^{-}\otimes\boldsymbol{\Lambda}^{-} \tag{2.22}$$

8

for the second-order tensors $\boldsymbol{\Lambda}^{\pm} := \partial Y^{\pm}/\partial\bar{\boldsymbol{\sigma}}$. Note that upon damage unloading (i.e., $\dot{d}^{\pm} = 0$) it follows that $h^{\pm} = 0$.

Calling for the linear elastic relation (2.1), the constitutive relations (2.9) in rate form then read

$$\dot{\bar{\boldsymbol{\sigma}}} = \left(\mathbb{I} - \mathbb{Q} - \mathbb{H}\right) : \mathbb{E}_0 : \boldsymbol{\epsilon} = \mathbb{E}^{\text{tan}} : \dot{\boldsymbol{\epsilon}} \tag{2.23a}$$

for the tangent stiffness tensor $\mathbb{E}^{\text{tan}}$

$$\mathbb{E}^{\text{tan}} = \left(\mathbb{I} - \mathbb{Q} - \mathbb{H}\right) : \mathbb{E}_0 \tag{2.23b}$$

As can be seen, the material tangent $\mathbb{E}^{\text{tan}}$ is in general non-symmetric due to the damage evolution.

3. Analysis of the classical positive/negative projection (PNP)

In this section the classical PNP (Ortiz, 1985; Simó and Ju, 1987; Carol and Willam, 1996; Wu and Xu, 2013) is obtained from a variational point of view rather than proposed heuristically. Deficiencies of the resulting damage model are then addressed, showing the necessity of introducing a novel PNP.

3.1. Mathematic definition of the classical PNP

Let us consider the following PNP

$$\begin{cases} \bar{\boldsymbol{\sigma}} = \bar{\boldsymbol{\sigma}}^+ + \bar{\boldsymbol{\sigma}}^- \\ \bar{\boldsymbol{\sigma}}^+ \in \mathscr{C}^+ \\ \bar{\boldsymbol{\sigma}}^- \in \mathscr{C}^- \\ \bar{\boldsymbol{\sigma}}^+ : \bar{\boldsymbol{\sigma}}^- = \bar{\boldsymbol{\sigma}}^- : \bar{\boldsymbol{\sigma}}^+ = 0 \end{cases} \tag{3.1}$$

Compared to the general definition in Section 2.2, an extra orthogonal condition $(3.1)_4$ is imposed such that the corresponding positive/negative effective stress tensors $\bar{\boldsymbol{\sigma}}^{\pm}$ can be determined uniquely.

It can be proved that the PNP (3.1) is equivalent to the following variational inequality (see Appendix A for the proof)

$$\left(\bar{\boldsymbol{\sigma}}^+ - \boldsymbol{\Sigma}\right) : \left(\bar{\boldsymbol{\sigma}} - \bar{\boldsymbol{\sigma}}^+\right) \geq 0 \quad \forall \boldsymbol{\Sigma} \in \mathscr{C}^+ \qquad \Longleftrightarrow \qquad \bar{\boldsymbol{\sigma}}^+ = \text{Arg} \max_{\boldsymbol{\Sigma} \in \mathscr{C}^+} \boldsymbol{\Sigma} : \bar{\boldsymbol{\sigma}}^- \tag{3.2a}$$

or, equivalently,

$$\left(\bar{\boldsymbol{\sigma}}^- - \boldsymbol{\Sigma}\right) : \left(\bar{\boldsymbol{\sigma}} - \bar{\boldsymbol{\sigma}}^-\right) \geq 0 \quad \forall \boldsymbol{\Sigma} \in \mathscr{C}^- \qquad \Longleftrightarrow \qquad \bar{\boldsymbol{\sigma}}^- = \text{Arg} \max_{\boldsymbol{\Sigma} \in \mathscr{C}^-} \boldsymbol{\Sigma} : \bar{\boldsymbol{\sigma}}^+ \tag{3.2b}$$

That is, the PNP (3.1) maximizes the inner product $\boldsymbol{\Sigma} : \bar{\boldsymbol{\sigma}}^- \; \forall \boldsymbol{\Sigma} \in \mathscr{C}^+$ (or $\boldsymbol{\Sigma} : \bar{\boldsymbol{\sigma}}^+ \; \forall \boldsymbol{\Sigma} \in \mathscr{C}^-$), mimicking the postulate of maximum plastic dissipation (Simó and Hughes, 1998).

Furthermore, it follows from the convexity analysis (see Nguyen (2000), p.48) that the positive/negative effective stress tensors $\bar{\boldsymbol{\sigma}}^{\pm}$ satisfying the variational inequalities (3.2) exist and are uniquely determined by

$$\bar{\boldsymbol{\sigma}}^{\pm} = \text{Arg} \min_{\boldsymbol{\Sigma} \in \mathscr{C}^{\pm}} \|\bar{\boldsymbol{\sigma}} - \boldsymbol{\Sigma}\|_F \tag{3.3}$$

for the Frobenius or Hilbert-Schmidt norm $\|\bar{\boldsymbol{\sigma}} - \boldsymbol{\Sigma}\|_F := \left[(\bar{\boldsymbol{\sigma}} - \boldsymbol{\Sigma}) : (\bar{\boldsymbol{\sigma}} - \boldsymbol{\Sigma})\right]^{1/2}$. Namely, the positive effective stress tensor $\bar{\boldsymbol{\sigma}}^+$ (or the negative one $\bar{\boldsymbol{\sigma}}^-$) is the closest point (orthogonal) projection of the effective stress tensor $\bar{\boldsymbol{\sigma}}$ onto the non-negative cone $\mathscr{C}^+$ (or the non-positive one $\mathscr{C}^-$).

The property $(3.1)_4$ verifies that the positive/negative components $\bar{\boldsymbol{\sigma}}^{\pm}$ are indeed coaxial to the effective stress tensor $\bar{\boldsymbol{\sigma}}$ (and also to the strain tensor $\boldsymbol{\epsilon}$) as expected; see Lemma 1 of Appendix A. This coaxiality between $\bar{\boldsymbol{\sigma}}^+$ and $\bar{\boldsymbol{\sigma}}^-$ greatly simplifies the solution procedure since only the principal values need to be considered for the orthogonality condition $(3.1)_4$, i.e.,

$$\bar{\boldsymbol{\sigma}}^+ : \bar{\boldsymbol{\sigma}}^- = \sum_n \bar{\sigma}_n^+ \bar{\sigma}_n^- = 0 \qquad \Longrightarrow \qquad \bar{\sigma}_n^+ \bar{\sigma}_n^- = \bar{\sigma}_n^+ (\bar{\sigma}_n - \bar{\sigma}_n^+) = 0 \tag{3.4}$$

for the eigenvalues $\bar{\sigma}_n^+ \geq 0$ and $\bar{\sigma}_n^- \leq 0$ with opposite signs by definition.

From the condition (3.4), the positive/negative components $\bar{\sigma}_n^{\pm}$ can be trivially solved as

$$\bar{\sigma}_n^+ = \begin{cases} \bar{\sigma}_n & \bar{\sigma}_n \geq 0 \\ 0 & \bar{\sigma}_n \leq 0 \end{cases} \quad \text{and} \quad \bar{\sigma}_n^- = \bar{\sigma}_n - \bar{\sigma}_n^+ = \begin{cases} 0 & \bar{\sigma}_n \geq 0 \\ \bar{\sigma}_n & \bar{\sigma}_n \leq 0 \end{cases} \tag{3.5a}$$

or, equivalently,

$$\bar{\sigma}_n^+ = \langle \bar{\sigma}_n \rangle = \boldsymbol{P}_{nn}^+ : \bar{\boldsymbol{\sigma}}, \qquad \bar{\sigma}_n^- = \bar{\sigma}_n - \langle \bar{\sigma}_n \rangle = -\langle -\bar{\sigma}_n \rangle = \boldsymbol{P}_{nn}^- : \bar{\boldsymbol{\sigma}} \tag{3.5b}$$

where the second-order symmetric tensors $\boldsymbol{P}_{nn}^{\pm}$ introduced in Eq. (2.5) are given by

$$\boldsymbol{P}_{nn}^+ = H(\bar{\sigma}_n) \boldsymbol{P}_{nn}, \qquad \boldsymbol{P}_{nn}^- = H(-\bar{\sigma}_n) \boldsymbol{P}_{nn} \tag{3.6}$$

Accordingly, the irreducible PNP operators $\mathbb{P}^{\pm}$ read

$$\mathbb{P}^+ = \sum_{n=1}^{3} H(\bar{\sigma}_n) \boldsymbol{P}_{nn} \otimes \boldsymbol{P}_{nn}, \qquad \mathbb{P}^- = \mathbb{I} - \mathbb{P}^+ \tag{3.7}$$

which possess both *major and minor symmetries*.

As can be seen, the PNP (3.1) corresponds exactly to the classical one first adopted by those French scholars in the modeling of concrete; see Mazars and Pijaudier-Cabot (1989) for the review. It is in Ortiz (1985) that the PNP operators (3.7) were first used to develop an anisotropic damage model for concrete. Ever since then, the classical PNP has been dominantly employed in the literature. Several different expressions for the PNP operators (Simó and Ju, 1987; Carol and Willam, 1996) were proposed to overcome the deficiencies exhibited by the irreducible ones (3.7). Recently, all the classical PNP operators were incorporated into a unified form (Wu and Xu, 2013) and the thermodynamically consistent expressions (2.19) were derived to guarantee zero energy dissipation for any closed loading cycle.

3.2. Analysis of the resulting damage model

With the classical PNP (3.1), the additive bi-scalar damage theory presented in Section 2 recovers the model proposed in Cervera et al. (1995); Faria et al. (1998) and developed further by Wu et al. (2006). Though it has been widely adopted in the modeling of concrete (Li and Ren, 2009; Gernay et al., 2013; Grassl et al., 2013) and masonry (Pelà et al., 2011), this model exhibits two noteworthy deficiencies.

Firstly, the model gives an unrealistic prediction of excessive lateral deformations under uniaxial tension. It is known that, a crack generation under uniaxial tension is accompanied with strain localization in that direction, resulting in elastic unloading in the lateral orientation (Ožbolt et al., 2001; Wu and Cervera, 2017). This structural effect can be correctly accounted for by smeared crack models (Rots et al., 1985) and anisotropic damage models (Carol et al., 2001; Wu and Xu, 2011), but not by the current one with the classical PNP (3.1). The reason is that the stress-strain relation (2.9a) is isotropic for uniaxial tension

$$\bar{\boldsymbol{\sigma}}^+ = \bar{\boldsymbol{\sigma}}, \qquad \bar{\boldsymbol{\sigma}}^- = \boldsymbol{0} \qquad \Longrightarrow \qquad \boldsymbol{\sigma} = (1 - d^+)\bar{\boldsymbol{\sigma}} \tag{3.8}$$

which implies a constant nominal Poisson's ratio throughout the loading history (Ju, 1990)

$$\nu := -\frac{\epsilon_3}{\epsilon_1} = \nu_0 \tag{3.9}$$

Accordingly, the lateral contraction ϵ_3 would continue increasing as the axial elongation ϵ_1 does, conflicting with the unloading lateral behavior of quasi-brittle materials; see Section 6.1.1 for the numerical results. Note that the Mazars and Pijaudier-Cabot (1989) damage model (2.14) exhibits the same issue.

Secondly, for the classical PNP operators (3.7) the secant stiffness (2.9b) and compliance (2.13a)$_2$ in general are not (major) symmetric. This fact can be seen from the following results

$$\mathbb{P}^\pm : \mathbb{E}_0 = 2G_0\big(\mathbb{P}^\pm + \hat{\nu}_0 \boldsymbol{I}^\pm \otimes \boldsymbol{I}\big), \qquad \mathbb{C}_0 : \mathbb{P}^\pm = \frac{1}{E_0}\Big[(1 + \nu_0)\mathbb{P}^\pm - \nu_0 \boldsymbol{I} \otimes \boldsymbol{I}^\pm\Big] \tag{3.10}$$

with the second-order symmetric tensors $\boldsymbol{I}^\pm := \sum_n H(\pm\bar{\sigma}_n)\boldsymbol{P}_{nn}$. Only for states of pure tension or pure compression, in which the relations $\boldsymbol{I}^\pm = \boldsymbol{I}$ hold, can the major symmetry of the secant stiffness (or compliance) tensor be guaranteed. Though this fact does not necessarily lead to the violation of thermodynamics (Carol and Willam, 1996), a well-defined Helmholtz or Gibbs free energy potential cannot be postulated. Consequently, the resulting damage model cannot be cast in the framework of thermodynamics with internal variables.

Remark 3.1 For the Mazars and Pijaudier-Cabot (1989) damage model, the secant compliance (2.14b) is always of major symmetry, provided that the PNP operators are symmetric. Therefore, the classical PNP operators (3.7) sufficiently guarantee the existence of a well-defined free energy potential. However, the issue of excessive lateral deformations is still exhibited. Furthermore, a unilateral damage model based on the PNP of the stress tensor is numerically cumbersome (Mahnken et al., 2000). □

11

4. Novel positive/negative projection (PNP) in energy norm

As the resulting stiffness tensor is not of major symmetry, the classical PNP scheme is not optimal for the current additive bi-scalar damage theory. However, the PNP scheme and the associated projection operators are not unique, and it is thus possible to construct an alternative optimal one. In this section, we introduce such a novel PNP scheme of the effective stress tensor. Its variational interpretation and the explicit solution are presented. With this novel projection, the major symmetry of the resulting stiffness and compliance tensors is guaranteed. Furthermore, the issue of excessive lateral deformations under uniaxial tension is also removed.

4.1. Closest-point PNP in energy norm

Let us consider the following PNP scheme

$$
\begin{cases}
\bar{\boldsymbol{\sigma}} = \bar{\boldsymbol{\sigma}}^+ + \bar{\boldsymbol{\sigma}}^- \\
\bar{\boldsymbol{\sigma}}^- \in \mathscr{C}^- \\
\boldsymbol{\epsilon}^+ := \mathbb{C}_0 : \bar{\boldsymbol{\sigma}}^+ \in \mathscr{C}^+ \quad \implies \quad \bar{\boldsymbol{\sigma}}^+ := \mathbb{E}_0 : \boldsymbol{\epsilon}^+ \in \mathscr{C}^+ \\
\bar{\boldsymbol{\sigma}}^+ : \mathbb{C}_0 : \bar{\boldsymbol{\sigma}}^- = \bar{\boldsymbol{\sigma}}^- : \mathbb{C}_0 : \bar{\boldsymbol{\sigma}}^+ = 0
\end{cases}
\tag{4.1}
$$

Compared to the classical PNP scheme (3.1), here the orthogonal condition $(4.1)_4$ in energy norm is considered. Note that, as all the coefficients in the elasticity tensor $(2.2)_1$ are non-negative for $\nu_0 \in [-1, 0.5]$, the condition $(4.1)_3$, i.e., $\boldsymbol{\epsilon}^+ \in \mathscr{C}^+$, intrinsically implies $\bar{\boldsymbol{\sigma}}^+ \in \mathscr{C}^+$. However, the inverse argument does not hold since some coefficients in the compliance tensor $(2.2)_2$ are negative. For instance, the relation $(4.1)_2$, i.e., $\bar{\boldsymbol{\sigma}}^- \in \mathscr{C}^-$, does not imply $\mathbb{C}_0 : \bar{\boldsymbol{\sigma}}^- \in \mathscr{C}^-$; see Remark 4.1 for a spurious PNP introduced in no-tension materials (Del Piero, 1989; Alfano et al., 2000).

Before the explicit solution to the projection (4.1) is derived, the following proposition is first presented.

Proposition 1 The PNP scheme (4.1) can be alternatively expressed as

$$
\left(\bar{\boldsymbol{\sigma}}^- - \boldsymbol{\Sigma}\right) : \mathbb{C}_0 : \left(\bar{\boldsymbol{\sigma}} - \bar{\boldsymbol{\sigma}}^-\right) \geq 0 \quad \forall \boldsymbol{\Sigma} \in \mathscr{C}^- \quad \iff \quad \bar{\boldsymbol{\sigma}}^- = \operatorname*{Arg\,max}_{\boldsymbol{\Sigma} \in \mathscr{C}^-} \boldsymbol{\Sigma} : \boldsymbol{\epsilon}^+
\tag{4.2a}
$$

or, equivalently,

$$
\left(\boldsymbol{\epsilon}^+ - \boldsymbol{\Gamma}\right) : \mathbb{E}_0 : \left(\boldsymbol{\epsilon} - \boldsymbol{\epsilon}^+\right) \geq 0 \quad \forall \boldsymbol{\Gamma} \in \mathscr{C}^+ \quad \iff \quad \mathbb{C}_0 : \bar{\boldsymbol{\sigma}}^+ = \operatorname*{Arg\,max}_{\boldsymbol{\Gamma} \in \mathscr{C}^+} \boldsymbol{\Gamma} : \bar{\boldsymbol{\sigma}}^-
\tag{4.2b}
$$

The proof is given in Appendix A. Proposition 1 mimics the classical postulate of maximum plastic dissipation (Simó and Hughes, 1998) in which the plastic strain rate is replaced by the positive strain tensor $\boldsymbol{\epsilon}^+ := \mathbb{C}_0 : \bar{\boldsymbol{\sigma}}^+$.

The positive/negative effective stress tensors $\bar{\boldsymbol{\sigma}}^\pm$ determined by the PNP scheme (4.1) or the variational inequality (4.2) also satisfy the following minimization problem (see Nguyen (2000), p.48 for the details)

$$
\bar{\boldsymbol{\sigma}}^- = \operatorname*{Arg\,min}_{\boldsymbol{\Sigma} \in \mathscr{C}^-} \frac{1}{2} \|\bar{\boldsymbol{\sigma}} - \boldsymbol{\Sigma}\|_{\mathbb{C}_0} = \operatorname*{Arg\,min}_{\boldsymbol{\Sigma} \in \mathscr{C}^-} \frac{1}{2} \left(\bar{\boldsymbol{\sigma}} - \boldsymbol{\Sigma}\right) : \mathbb{C}_0 : \left(\bar{\boldsymbol{\sigma}} - \boldsymbol{\Sigma}\right)
\tag{4.3a}
$$

or, equivalently,

$$\mathbb{C}_0 : \bar{\boldsymbol{\sigma}}^+ = \text{Arg} \min_{\boldsymbol{\Gamma} \in \mathscr{C}^+} \frac{1}{2} \|\boldsymbol{\epsilon} - \boldsymbol{\Gamma}\|_{\mathbb{E}_0} = \text{Arg} \min_{\boldsymbol{\Gamma} \in \mathscr{C}^+} \frac{1}{2} (\boldsymbol{\epsilon} - \boldsymbol{\Gamma}) : \mathbb{E}_0 : (\boldsymbol{\epsilon} - \boldsymbol{\Gamma}) \tag{4.3b}$$

The minimization problem (4.3) states that the negative effective stress tensor $\bar{\boldsymbol{\sigma}}^-$ (or the strain $\mathbb{C}_0 : \bar{\boldsymbol{\sigma}}^+$ associated with the positive effective stress tensor $\bar{\boldsymbol{\sigma}}^+$) is the closest point projection onto the space $\mathscr{C}^-$ (or $\mathscr{C}^+$) of the effective stress tensor $\bar{\boldsymbol{\sigma}}$ (or the strain tensor $\boldsymbol{\epsilon}$) in energy form induced by the compliance tensor $\mathbb{C}_0$ (or the stiffness tensor $\mathbb{E}_0$). This variational interpretation is different from that of the classical PNP scheme (3.1) in which the Frobenius norm is considered.

Interestingly, the above variational argument is very similar to the closest point projection based return mapping algorithm used in computational inelasticity (Simó and Hughes, 1998). In particular, for the effective stress space plasticity (Ju, 1989; Wu et al., 2006) the solution is the closest point projection on the admissible (yield) surface of the elastic trial stress tensor in the same energy form.

Remark 4.1 The PNP scheme (4.1) is similar to the definition of no-tension masonry-like materials (Del Piero, 1989; Alfano et al., 2000; Freddi and Royer-Carfagni, 2010; Li et al., 2016). In these references, the decomposition is performed to the strain tensor $\boldsymbol{\epsilon}$, resulting in a *spurious* negative component $\mathbb{C}_0 : \bar{\boldsymbol{\sigma}}^- \notin \mathscr{C}^-$ which is inconsistent with the definition (2.4). $\square$

4.2. Explicit solution of the PNP in energy norm

Similarly, convexity analysis guarantees the existence and uniqueness of the solution to the PNP scheme (4.1) or the equivalent minimization problem (4.3). The property (4.1)$_4$ also ensues the coaxility between the positive/negative components $\bar{\boldsymbol{\sigma}}^\pm$ and the effective stress tensor $\bar{\boldsymbol{\sigma}}$. Accordingly, the closest point (orthogonal) projection (4.1) in energy norm is expressed in terms of the principal values as

$$\bar{\boldsymbol{\sigma}}^- : \boldsymbol{\epsilon}^+ = \sum_n \bar{\sigma}_n^- \epsilon_n^+ = 0 \tag{4.4}$$

As the eigenvalues $\bar{\sigma}_n^- \leq 0$ of the negative effective stress tensor $\bar{\boldsymbol{\sigma}}^-$ and $\epsilon_n^+ \geq 0$ of the strain tensor $\boldsymbol{\epsilon}^+ = \mathbb{C}_0 : (\bar{\boldsymbol{\sigma}} - \bar{\boldsymbol{\sigma}}^-)$ are of opposite signs by definition, it follows that

$$\bar{\sigma}_n^- \epsilon_n^+ \equiv 0 \qquad \Longleftrightarrow \qquad \bar{\sigma}_n^- = 0 \quad \text{or} \quad \epsilon_n^+ = 0 \tag{4.5a}$$

or, equivalently,

$$\begin{cases} \dfrac{1}{E_0} \bar{\sigma}_1^- \left[\bar{\sigma}_1^+ - \nu_0 (\bar{\sigma}_2^+ + \bar{\sigma}_3^+) \right] = 0 \\[2mm] \dfrac{1}{E_0} \bar{\sigma}_2^- \left[\bar{\sigma}_2^+ - \nu_0 (\bar{\sigma}_1^+ + \bar{\sigma}_3^+) \right] = 0 \\[2mm] \dfrac{1}{E_0} \bar{\sigma}_3^- \left[\bar{\sigma}_3^+ - \nu_0 (\bar{\sigma}_1^+ + \bar{\sigma}_2^+) \right] = 0 \end{cases} \tag{4.5b}$$

where the constitutive relation $(2.1)_2$ has been applied in the principal space.

With the complementary conditions $\bar{\sigma}_n^+ = \bar{\sigma}_n - \bar{\sigma}_n^-$, the following solution is obtained from Eq. (4.5b)

$$\bar{\sigma}_1^+ = \langle \bar{\sigma}_1 \rangle \tag{4.6a}$$

$$\bar{\sigma}_2^+ = \Big\langle \max\big(\bar{\sigma}_2, \tilde{v}_0 \bar{\sigma}_1\big) \Big\rangle, \quad \bar{\sigma}_3^+ = \Big\langle \max\big[\max\big(\bar{\sigma}_3, v_0(\bar{\sigma}_1 + \bar{\sigma}_2)\big), \tilde{v}_0 \bar{\sigma}_1\big] \Big\rangle \tag{4.6b}$$

for the parameter $\tilde{v}_0 := v_0/(1 - v_0)$; see Appendix B for the details. As can be seen, only the major principal value $\bar{\sigma}_1^+$ coincides with that of the classical PNP, but the intermediate and minor ones are different.

For the plane stress condition (the out-of-plane stress $\bar{\sigma}_2 = 0$), the above results also apply with $\bar{\sigma}_2$ neglected, i.e.,

$$\bar{\sigma}_1^+ = \langle \bar{\sigma}_1 \rangle, \qquad \bar{\sigma}_2^+ = 0, \qquad \bar{\sigma}_3^+ = \Big\langle \max\big(\bar{\sigma}_3, v_0 \bar{\sigma}_1\big) \Big\rangle \tag{4.7}$$

The above results are illustrated in Figure 1.

Calling for the relation $(2.3)_2$, the second-order symmetric tensors $\boldsymbol{P}_{nn}^+$ associated with the positive principal values $\bar{\sigma}_n^+$ are expressed as

$$\begin{cases} \boldsymbol{P}_{11}^+ = \boldsymbol{P}_{11}, \ \boldsymbol{P}_{22}^+ = \boldsymbol{P}_{22}, \ \boldsymbol{P}_{33}^+ = \boldsymbol{P}_{33} & \text{Case \ I}: \ \bar{\sigma}_1 \geq 0, \ \bar{\sigma}_2 \geq 0, \ \bar{\sigma}_3 \geq v_0(\bar{\sigma}_1 + \bar{\sigma}_2) \\ \boldsymbol{P}_{11}^+ = \boldsymbol{P}_{11}, \ \boldsymbol{P}_{22}^+ = \boldsymbol{P}_{22}, \ \boldsymbol{P}_{33}^+ = v_0(\boldsymbol{P}_{11} + \boldsymbol{P}_{22}) & \text{Case \ II}: \ \bar{\sigma}_1 \geq 0, \ \bar{\sigma}_2 \geq 0, \ \bar{\sigma}_3 \leq v_0(\bar{\sigma}_1 + \bar{\sigma}_2) \\ \boldsymbol{P}_{11}^+ = \boldsymbol{P}_{11}, \ \boldsymbol{P}_{22}^+ = \boldsymbol{P}_{33}^+ = \tilde{v}_0 \boldsymbol{P}_{11} & \text{Case III}: \ \bar{\sigma}_1 \geq 0, \ \bar{\sigma}_3 \leq \bar{\sigma}_2 \leq \tilde{v}_0 \bar{\sigma}_1 \\ \boldsymbol{P}_{11}^+ = \boldsymbol{P}_{22}^+ = \boldsymbol{P}_{33}^+ = \boldsymbol{0} & \text{Case IV}: \ \bar{\sigma}_3 \leq \bar{\sigma}_2 \leq \bar{\sigma}_1 \leq 0 \end{cases} \tag{4.8}$$

The corresponding PNP operators $\mathbb{P}^\pm$ are then given by Eqs. (2.7).

With the above PNP in energy norm, it is verified in Appendix C that the stiffness tensor $\mathbb{E}$ (and compliance $\mathbb{C}$) given in Eq. (2.9b) are always major symmetric. Accordingly, a unique free energy potential can be well defined such that the resulting additive bi-scalar damage model can be cast into the thermodynamics framework with internal variables. This topic is deferred to Section 5.

Remark 4.2 The additive bi-scalar damage model with the novel PNP predicts orthotropic material behavior under mixed tension/compression (Cases II and III). In particular, under uniaxial tension ($\sigma_2 = \sigma_3 = 0$), it follows from the relation (C.3) and $d^- = 0$ that

$$\sigma_3 = \bar{\sigma}_3 - d^+ v_0 \bar{\epsilon}_1 = \frac{v_0 E_0}{1 - v_0^2}\Big[(1 - d^+)v_0 \epsilon_1 + (1 - d^+ v_0^2)\epsilon_3\Big] = 0 \tag{4.9}$$

or, equivalently,

$$v := -\frac{\epsilon_3}{\epsilon_1} = \frac{1 - d^+}{1 - d^+ v_0^2} v_0, \qquad \sigma_1 = \frac{1 - d^+}{1 - d^+ v_0^2} E_0 \epsilon_1 \tag{4.10}$$

As can be seen, the nominal Poisson's ratio v decreases progressively to zero once damage is initiated, completely removing the excessive lateral deformations exhibited in the model with the classical positive/negative projection. $\square$

Remark 4.3 Another approach to face the issues underlined in Section 3.2 was recently proposed by Cervera and Tesei (2017). They formulated a multiplicative bi-scalar damage model with stiffness tensor of major symmetry based

14

on the postulate of energy equivalence (Cordebois and Sidoroff, 1982; Carol et al., 2001) and on the decomposition of the strain tensor. In this way, an improved representation of Poisson's ratio effect with respect to the damage theory presented in Section 2 is also obtained. In order that the strain-driven numerical algorithm can still be used, the classical PNP is performed on the strain tensor. Accordingly, the flexibility of accounting for plastic strains through the effective stress tensor (2.1) and the conceptually sound constitutive relations (2.9), both contributing to success of the original additive bi-scalar damage model, are not maintained.

5. Thermodynamics framework

With the closest point (orthogonal) PNP in energy form, the effective stress based additive bi-scalar damage theory presented in Section 2 can now be cast into the framework of thermodynamics with internal variables. In particular, the damage criteria and evolution laws are established consistently based on the damage energy release rates.

5.1. Moreau's decomposition of the free energy potential

As usual, the initial Helmholtz free energy (HFE) potential of a damaging solid is defined as the strain energy potential of the virgin material, i.e.,

$$\psi_0(\bar{\sigma}) = \frac{1}{2}\epsilon : \mathbb{E}_0 : \epsilon = \frac{1}{2}\bar{\sigma} : \mathbb{C}_0 : \bar{\sigma} \tag{5.1}$$

The closest point (orthogonal) projection (4.1) in energy norm admits the Moreau's decomposition (Moreau, 1974) of the elastic strain energy potential ψ_0

$$\psi_0(\bar{\sigma}) = \psi_0^+(\bar{\sigma}^+) + \psi_0^-(\bar{\sigma}^-) \tag{5.2a}$$

with the following positive/negative components

$$\psi_0^\pm(\bar{\sigma}^\pm) = \frac{1}{2}\bar{\sigma}^\pm : \mathbb{C}_0 : \bar{\sigma} = \frac{1}{2}\bar{\sigma}^\pm : \mathbb{C}_0 : \bar{\sigma}^\pm \tag{5.2b}$$

Note that the above decomposition does not hold for the classical PNP scheme (3.1); see Remark 5.1. Calling for the variational argument (4.3), it follows that the negative effective stress tensor $\bar{\sigma}^-$ (or the positive strain tensor $\mathbb{C}_0 : \bar{\sigma}^+$) minimizes the positive part ψ_0^+ (or the negative one ψ_0^-) of the elastic strain energy ψ_0.

Accordingly, the HFE potential ψ of the damaging solid is characterized by the damage variables $d^+ \in [0, 1]$ and $d^- \in [0, 1]$ as follows

$$\psi(\epsilon, d^+, d^-) = (1 - d^+)\psi_0^+(\bar{\sigma}^+) + (1 - d^-)\psi_0^-(\bar{\sigma}^-) \tag{5.3}$$

As the major symmetry of the resulting stiffness tensor $\mathbb{E}$ is always guaranteed for the novel PNP (4.1) in energy norm, the corresponding HFE potential function (5.3) is uniquely defined.

Remark 5.1 For the classical PNP scheme (3.1), the orthogonal condition in energy norm does not hold

$$\bar{\sigma}^+ : \mathbb{C}_0 : \bar{\sigma}^- = -\frac{1}{E_0}\nu_0 \text{tr}\,\bar{\sigma}^+\,\text{tr}\,\bar{\sigma}^- \neq 0 \tag{5.4}$$

That is, the cross term in the free energy potential ψ_0 does not vanish and the second equation in Eq. (5.2b) does not hold any more. Consequently, the positive component of the initial HFE potential ψ_0^+ (or the negative one ψ_0^-) cannot be expressed in terms of the corresponding individual component $\bar{\sigma}^+$ (or $\bar{\sigma}^-$) of the effective stress, resulting in loss of major symmetry of the stiffness tensor and non-existence of a well-defined free energy potential. This issue is removed in this work with the novel PNP in energy norm. □

5.2. Thermodynamically consistent constitutive relations

For any arbitrary deformation process, the first and second laws of thermodynamics have to be satisfied, i.e.,

$$\dot{\mathscr{D}} = \boldsymbol{\sigma} : \dot{\boldsymbol{\epsilon}} - \dot{\psi} \geq 0 \tag{5.5}$$

Making standard arguments (Coleman and Gurtin, 1967) and assuming elastic unloading, yield

$$\boldsymbol{\sigma} = \frac{\partial \psi}{\partial \boldsymbol{\epsilon}} = \mathbb{E}_0 : \frac{\partial \psi}{\partial \bar{\boldsymbol{\sigma}}} = \left(1 - d^+\right)\frac{\partial \bar{\boldsymbol{\sigma}}^+}{\partial \bar{\boldsymbol{\sigma}}} : \bar{\boldsymbol{\sigma}}^+ + \left(1 - d^-\right)\frac{\partial \bar{\boldsymbol{\sigma}}^-}{\partial \bar{\boldsymbol{\sigma}}} : \bar{\boldsymbol{\sigma}}^- \tag{5.6}$$

or, equivalently, in the form (2.9)

$$\boldsymbol{\sigma} = \left(1 - d^+\right)\mathbb{Q}^+ : \bar{\boldsymbol{\sigma}}^+ + \left(1 - d^-\right)\mathbb{Q}^- : \bar{\boldsymbol{\sigma}}^- = \left(1 - d^+\right)\bar{\boldsymbol{\sigma}}^+ + \left(1 - d^-\right)\bar{\boldsymbol{\sigma}}^- \tag{5.7}$$

where the relations $\mathbb{Q}^\pm : \bar{\boldsymbol{\sigma}}^\pm = \bar{\boldsymbol{\sigma}}^\pm$ resulting from the properties (2.8) and (2.20) have been considered for the thermodynamically consistent PNP operators $\mathbb{Q}^\pm$.

Besides the above additive bi-scalar constitutive relation, the following damage dissipation inequality holds

$$\dot{\mathscr{D}} = -\frac{\partial \psi}{\partial d^+}\dot{d}^+ - \frac{\partial \psi}{\partial d^-}\dot{d}^- = Y^+\dot{d}^+ + Y^-\dot{d}^- \geq 0 \tag{5.8a}$$

or, more strictly,

$$\dot{\mathscr{D}}^+ = Y^+\dot{d}^+ \geq 0, \qquad \dot{\mathscr{D}}^- = Y^-\dot{d}^- \geq 0 \tag{5.8b}$$

where the dissipations $\dot{\mathscr{D}}^+$ and $\dot{\mathscr{D}}^-$ under pure tension/compression are assumed to be decoupled.

The thermodynamic forces (i.e., the damage energy release rates), Y^+ and Y^-, conjugate to the damage variables d^+ and d^-, respectively, are expressed as

$$Y^\pm = -\frac{\partial \psi}{\partial d^\pm} = \psi_0(\bar{\boldsymbol{\sigma}}^\pm) = \frac{1}{2}\bar{\boldsymbol{\sigma}}^\pm : \mathbb{C}_0 : \bar{\boldsymbol{\sigma}}^\pm = \frac{1}{2E_0}\left[\left(1 + \nu_0\right)\bar{\boldsymbol{\sigma}}^\pm : \bar{\boldsymbol{\sigma}}^\pm - \nu_0 \text{tr}^2\bar{\boldsymbol{\sigma}}^\pm\right] \tag{5.9}$$

Accordingly, the damage criteria $g^\pm(Y^\pm, r^\pm) \leq 0$ are determined by Eq. (2.15).

To gain further insights, let us consider the case of plane stress ($\bar{\sigma}_2 = 0$) in which the damage forces $Y^\pm$ become

$$Y^\pm = \frac{1}{2E_0}\left[\left(\bar{\sigma}_1^\pm\right)^2 + \left(\bar{\sigma}_3^\pm\right)^2 - 2\nu_0\bar{\sigma}_1^\pm\bar{\sigma}_3^\pm\right] \tag{5.10}$$

16

or, equivalently,

$$Y^+ = \begin{cases} \dfrac{1}{2E_0}\big(\bar{\sigma}_1^2 + \bar{\sigma}_3^2 - 2\nu_0\bar{\sigma}_1\bar{\sigma}_3\big) & \bar{\sigma}_1 \geq 0,\ \bar{\sigma}_3 \geq \nu_0\bar{\sigma}_1 \\[2ex] \dfrac{1-\nu_0^2}{2E_0}\bar{\sigma}_1^2 & \bar{\sigma}_1 \geq 0,\ \bar{\sigma}_3 \leq \nu_0\bar{\sigma}_1 \\[2ex] 0 & \bar{\sigma}_3 \leq \bar{\sigma}_1 \leq 0 \end{cases} \tag{5.11a}$$

$$Y^- = \begin{cases} 0 & \bar{\sigma}_1 \geq 0,\ \bar{\sigma}_3 \geq \nu_0\bar{\sigma}_1 \\[2ex] \dfrac{1}{2E_0}\big(\bar{\sigma}_3 - \nu_0\bar{\sigma}_1\big)^2 & \bar{\sigma}_1 \geq 0,\ \bar{\sigma}_3 \leq \nu_0\bar{\sigma}_1 \\[2ex] \dfrac{1}{2E_0}\big(\bar{\sigma}_1^2 + \bar{\sigma}_3^2 - 2\nu_0\bar{\sigma}_1\bar{\sigma}_3\big) & \bar{\sigma}_3 \leq \bar{\sigma}_1 \leq 0 \end{cases} \tag{5.11b}$$

For the cases of uniaxial tension ($\bar{\sigma}_1 > 0, \bar{\sigma}_2 = \bar{\sigma}_3 = 0$) and uniaxial compression ($\bar{\sigma}_1 = \bar{\sigma}_2 = 0, \bar{\sigma}_3 < 0$), by calling for the relations (B.1b) and (B.1d), the damage thresholds $r_0^{\pm}$ are then determined as

$$r_0^+ = \frac{1-\nu_0^2}{2E_0}\big(f_0^+\big)^2, \qquad r_0^- = \frac{1}{2E_0}\big(f_0^-\big)^2 \tag{5.12}$$

for the elastic limit strengths $f_0^{\pm} \geq 0$ under uniaxial tension and compression.

The resulting initial admissible (elastic) domain, defined by $g_0^{\pm} = Y^{\pm} - r_0^{\pm} \leq 0$, is shown in Figure 2. On the one hand, under biaxial tension and mixed tension/compression, the material behavior is characterized by a rounded-Rankine criterion appropriate for quasi-brittle solids like concrete. On the other hand, the strength under biaxial compression is under-estimated since the plastic flows are not considered. As for the pure compression state the novel PNP scheme coincides the classical one, the approach proposed in Wu et al. (2006) can be employed to account for the influences of plastic flows. This extension will be addressed elsewhere.

6. Numerical examples

In this section, the additive bi-scalar damage model with the novel projection is applied to several numerical examples. In all simulations, the plane stress state is assumed with $\sigma_2 = 0$.

For simplicity, only tensile damage is considered in later numerical examples, with the compressive one inactivated by simply setting $d^- = 0$. Though other functions can be considered, the tensile damage variable $d^+(r^+)$ is postulated as the following exponential function

$$d^+(r^+) = 1 - \sqrt{r_0^+/r^+}\ \exp\left[B^+\left(1 - \sqrt{r^+/r_0^+}\right)\right] \tag{6.1}$$

Under uniaxial tension ($\sigma_1 > 0$), the stress-strain relation is given from Eq. (4.10) as

$$\sigma_1 = \frac{1-d^+}{1-d^+\nu_0^2}E_0\epsilon_1 \approx \big(1-d^+\big)E_0\epsilon_1 \tag{6.2}$$

where the approximation in the second relation induces negligible errors.

17

However, the resulting constitutive relation with softening regimes cannot be directly used in the finite element analysis; otherwise the numerical results depend heavily on the mesh size. Though other nonlocal and gradient-enhanced methods (Pijaudier-Cabot and Bažant, 1987; Peerlings et al., 1996) can also be used to regularize the above local material model, it is generally accepted that the crack band model (Bažant and Oh, 1983) is adequate to mitigate the above concern for many practical purposes. In this approach, the stress-strain curve under uniaxial tension is adjusted in accordance with the element size such that

$$\int_0^\infty \sigma_1(\epsilon)\, \mathrm{d}\epsilon = \frac{G_{\mathrm{f}}}{l_{\mathrm{ch}}} = g_{\mathrm{f}} \tag{6.3}$$

where the so-called fracture energy G_{f}, usually regarded as a material property, is introduced to represent the energy required to open a unit area of crack; $g_{\mathrm{f}} := G_{\mathrm{f}}/l_{\mathrm{ch}}$ is the specific fracture energy per characteristic length l_{ch} of the finite element. Substitution of the damage evolution law (6.1) and the uniaxia stress (6.2) yields (Cervera et al., 1995; Faria et al., 1998; Wu et al., 2006)

$$B^+ = \left(\frac{E_0 G_{\mathrm{f}}}{l_{\mathrm{ch}} f_t^2} - \frac{1}{2} \right)^{-1} = \left(\frac{E_0 g_{\mathrm{f}}}{f_t^2} - \frac{1}{2} \right)^{-1} > 0 \tag{6.4}$$

where the elastic limit f_0^+ is assumed as the uniaxial tensile strength f_t.

Note that the characteristic length l_{ch} depends on the element type and the quadrature scheme adopted. In the later numerical examples, the characteristic lengths $l_{\mathrm{ch}} = \sqrt{2}h$ for the standard displacement based elements (Rots, 1988) and $l_{\mathrm{ch}} = 2h$ for the mixed ones (Cervera et al., 2011) are considered, respectively, with h being the average mesh size.

6.1. Single-point examples

Several single-point examples are considered such that the stress-strain relations under typical load scenarios are calculated. In the numerical simulations, the material properties are assumed as follows: Young's modulus $E_0 = 30$ GPa, Poisson's ratio $\nu_0 = 0.2$, tensile strength $f_t = 3$ MPa.

6.1.1. Uniaxial tension

Let us first consider a single element subjected to uniaxial tension along axis x. For different values of the specific fracture energy g_{f}, the evolution curves of axial stress σ_{xx} *versus* axial strain ϵ_{xx} and lateral strain ϵ_{yy} are shown in Figure 3 for both the classical PNP scheme and the novel one. As can be clearly seen, the axial behavior predicted from the bi-scalar damage models with the classical PNP scheme and the novel one almost coincide. That is, a linear ascending branch is followed by an exponential softening regime approaching to zero asymptotically. As expected, a smaller g_{f} yields a steeper softening branch. However, the lateral predictions from both schemes are rather distinct. Namely, in pure tension the classical PNP scheme results in an isotropic damage model which exhibits excessive lateral deformations. Comparatively, the novel PNP scheme yields an orthotropic damage model, in which the lateral behavior remains elastic loading/unloading all along, without exhibiting excessive lateral contractions. The above results are consistent with the theoretical analyses detailed in Sections 3 and 4.

The above conclusion can be further demonstrated from Figure 4 which compares the evolution curves of the nominal Poisson's ratio. As can be seen, for the model with the PNP scheme the resulting nominal Poisson's ratio is constant as the initial value $\nu_0 = 0.2$ due to the excessive lateral deformations proportional to the axial ones. Contrariwise, regarding the damage model with the novel PNP scheme, as the axial strain increases, the nominal Poisson's ratio decreases from initial value $\nu_0 = 0.2$ asymptotically to zero. That is, as the axial strain approaches to infinity the lateral behavior does exhibit elastic unloading.

6.1.2. Pure distortion

Let us then consider the pure distortion. In this case, the major and minor principal strains are prescribed with the same intensity $\gamma/2 > 0$ and opposite signs

$$\epsilon_1 = \frac{\gamma}{2}, \qquad \epsilon_2 = 0, \qquad \epsilon_3 = -\frac{\gamma}{2} \tag{6.5}$$

Note that this strain state also applies to the simple shear.

Figure 5(a) shows the evolution curves of the normal stress σ_{xx} (or σ_{yy}) *versus* the shear strain ϵ_{xy}. As can be seen, the Reynolds effect, i.e, the presence of compressive normal stresses under shear strains, can be captured. The evolution curves of shear stress σ_{xy} *versus* shear strain ϵ_{xy} shown in Figure 5(b) can be explained by considering the maximum shear stress

$$\sigma_{xy} = \frac{\sigma_1 - \sigma_3}{2} \tag{6.6}$$

where the evolution curves of the principal stresses σ_1 and σ_3 are shown in Figures 5(c) and 5(d), respectively. The interaction between the softening major (tensile) principal stress σ_1 and the hardening minor (compressive) principal stress σ_3 leads to the shear stress σ_{xy} that exhibits initially softening but finally hardening behavior. As the shear strain approaches to infinity, the major principal stress σ_1 tends to zero, and shear stress simply becomes $\sigma_{xy} = -\sigma_3/2$. Similar predictions were also given by other anisotropic damage models (Carol et al., 2001; Wu and Xu, 2011).

6.1.3. Cyclic uniaxial tension/compression

The uniaxial cyclic tension/compression is then considered. As shown in Figure 6(a), during the first cycle, the material is stretched along axis x until the axial strain $\epsilon_{xx} = 1.5 \times 10^{-4}$ (in the softening region), compressed to $\epsilon_{xx} = -5.0 \times 10^{-4}$ and then unloads to zero; during the second one, the material is stretched to $\epsilon_{xx} = 2.5 \times 10^{-4}$, compressed again to $\epsilon_{xx} = -5.0 \times 10^{-4}$ and then unloads to zero; finally, the material is stretched until $\epsilon_{xx} = 5.0 \times 10^{-4}$. The specific fracture energy $g_f = 450\text{N/mm}^2$ is considered in the numerical simulation.

The evolution curve of axial stress σ_{xx} *versus* the prescribed axial strain ϵ_{xx} is shown in Figure 6(b). As can be seen, the material unloads along a straight line to the origin; upon load reversal, the previous stiffness (the initial elastic one) is recovered under compression; when the material is stretched again, the previous unloading path is followed during the reloading stage. That is, the microcracks closure-reopening effect, typical for concrete like quasi-brittle solids, can be well captured.

6.2. Benchmark examples under static loading

Several benchmark examples are considered. The mixed stabilized finite element P1P1 (Cervera et al., 2010a,b, 2011) are used in discretization of the computational domain, in order to suppress the mesh bias dependence and spurious stress locking notorious for orthotropic damage models. In all simulations the exponential function (6.1) is considered for the tensile damage d^+, with the parameter B^+ determined by Eq. (6.4). It is well-known that the crack band model is effective in suppressing the issue of mesh size dependence. For the mixed finite elements, the interested reader is referred to Barbat et al. (2017); Cervera et al. (2011, 2017) on this topic. As the meshes employed in the following numerical examples are almost coincident with those adopted in our recent work (Barbat et al., 2017; Cervera et al., 2017; Wu and Cervera, 2017), we only consider various mesh sizes in the first example.

Loading is applied by direct or indirect displacement control (de Borst, 1987). The Newton-Raphson method is used to solve the nonlinear system of equations arising from the spatial and temporal discretization of the problem. An automatic procedure is used to decide the step size and about 200 steps are necessary to complete the analyses. Convergence of a time step is attained when the ratio between the norms of the residual and the total forces is less than 10^{-3}. Calculations are performed with an enhanced version of the finite element program COMET (Cervera et al., 2002), developed at the International Center for Numerical Methods in Engineering (CIMNE). Pre- and post-processing is done with GiD, also developed at CIMNE (CIMNE, 2009).

6.2.1. Uniaxial stretch of a perforated strip

The first example is a 2D singly perforated strip loaded in uniaxial stretching via imposed vertical displacements at the top and bottom ends; horizontal movement is not restrained. Figure 7(a) depicts the geometry of the problem with dimensions 20 m × 40 m ×1 m (width × height × thickness). An imperfection is introduced with a slanted perforation of diameter $D = 1$ m such that symmetric solutions are excluded.

The following material properties are assumed: Youngs modulus $E_0 = 10$ MPa, tensile strength $f_t = 10$ KPa and fracture energy $G_f = 500$ J/m². Two values of Poissons ratio ν_0, i.e., $\nu = 0.0$ and $\nu_0 = 0.3$, are taken for comparison. As shown in Figures 7(b) and 7(c), two finite element meshes, i.e, the fine one with $h = 0.20$ m and coarse one with $h = 0.3$ m, respectively, are considered.

Using the fine mesh, the computed contours of displacement field and tensile damage are shown in Figure 8 for various Poisson's ratios. As expected, a horizontal localization band forms at the center of the strip in both cases, and the values of Poisson's ratio have no effect on the configuration of crack bands. Figure 9(a) compares the corresponding curves of applied force F^* and vertical displacement u^*. It can be seen that the lateral deformations due to non-vanishing Poisson's ratio have small but non-negligible effects on the softening regimes of global responses. For Poisson's ratio $\nu_0 = 0.3$, Figure 9(b) depicts the curves of applied force F^* and vertical displacement u^* for various mesh sizes. As can be seen, the crack band model is effective in guaranteeing the mesh size independence of global responses.

20

6.2.2. Single edge-notched beam under proportional loading (Arrea and Ingraffea, 1982)

Let us now consider the single edge-notched beams under proportional loading reported by Arrea and Ingraffea (1982). This pioneering work on mixed mode fracture is a good benchmark to verify concrete models.

In this work, only the concrete beams in series C are considered. The geometry, boundary and loading conditions of the tests are shown in Figure 10(a). The specimen was of dimension 1322 mm × 306 mm × 152 mm. A notch of depth 82 mm and out-of-plane thickness 152 mm was fabricated at the centroid of the bottom surface. As only two beams were tested, the experimental curves of load *versus* crack mouth shear displacement (CMSD) were very scattered. Furthermore, there are no data about the tensile strength f_t and the energy fracture G_f, both essential for defining the softening function. Due to the above facts, we do no intend to fit the global responses. In this work, the model properties given in Cendón et al. (2000), i.e., Young's modulus $E_0 = 2.48 \times 10^4$ MPa, Poisson's ratio $\nu_0 = 0.18$, the tensile strength $f_t = 3.7$ MPa and the fracture energy $G_f = 130$ J/m^2, are considered.

As shown in Figures 10(b) and 10(c) a refined mesh with an average size $h = 1$ mm is used to discretized the sub-domain encompassing potential crack paths. From our experiences this level of refinement is sufficient to guarantee convergence of the numerical simulation. The crack mouth sliding displacement (CMSD) is used to control the loading procedure.

The numerical damage contour is shown in Figure 11. As expected, the crack is initiated at the notch and then propagates along a curve line upwards to the right hand side of the cap where the load is applied. Figure 12 compares the numerical curves of load *versus* CMSD.

6.2.3. Single edge-notched beam under non-proportional loading (Gálvez et al., 1998)

The notched beams subjected to non-proportional loading reported in Gálvez et al. (1998) are considered next. Figure 13 depicts the geometry, boundary and loading conditions of the test. The beam is of dimensions 675 mm × 150 mm × 50 mm, with a vertical notch of sizes 2 mm × 75 mm × 50 mm at the bottom center. The beam was fixed at the right support (with a distance of 37.5 mm to the right end) and vertically constrained at the left support (with a distance of 75 mm to the central point). Depending on the stiffness of the spring at the left upper edge, the beam is subjected to either three-point ($k = 0$) or four-point ($k = \infty$) bending. The material properties are taken from Gálvez et al. (1998), i.e., Young's modulus $E_0 = 3.8 \times 10^4$ MPa, Poisson's ratio $\nu_0 = 0.2$, tensile strength $f_t = 3.0$ MPa and fracture energy $G_f = 69$ J/m^2.

Figure 13(b) and 13(c) depict the finite element mesh used in the numerical simulations, with a refined one of average size $h = 2.5$ mm around the sub-domain encompassing potential crack paths. The crack mouth opening displacement (CMOD) is used to control the loading procedure.

The numerically predicted damage contours are shown in Figures 14 and 15, both falling exactly within the experimental ranges of crack paths. It can be observed that the crack path changes significantly depending on the boundary conditions applied to the beam. Using an isotropic damage model, Cervera et al. (2010c) and Cervera et al. (2017) reported similar crack paths with a global tracking algorithm and with the mixed stabilized finite elements,

21

respectively.

Figures 16 and 17 show the load *versus* CMOD curves for both the three- and four-point bending tests. The results are similar to the ones obtained in Cervera et al. (2010c, 2017). In particular, the three-point bending test shows very good agreement with the experimental results, though the residual load capacity is slightly underestimated at the last stages of the simulation. The four-point bending test has its peak load slightly outside the experimental range of results. This occurs also in other references (Cervera et al., 2010c, 2017; Gálvez et al., 2000).

6.3. Concrete dam under earthquake excitation

During the earthquake motions in 1967, Koyna dam was subjected to both transverse and vertical components of the ground accelerations. This dam, extensively studied by other investigators (Bhattacharjee and Leeger, 1993; Ghrib and Tinawi, 1995; Cervera et al., 1995; Li and Fenves, 1998; Wu and Li, 2007), is finally considered.

Following the previous work, the dam-foundation interactions was ignored assuming a rigid foundation, and a finite element mesh consisting of 15455 standard piece-wise bilinear quadrilateral elements with reduced integration was adopted to discretize the dam. The dam-reservoir dynamic interactions were modeled using a 2-node element by the added mass technique of Westergaard (1933). A Rayleigh stiffness-proportional damping factor was assumed to provide a 3% fraction of the critical damping for the first vibration mode of the dam. The HHT-α method (Hilber et al., 1977) was considered to integrate the dynamic equation of motions. The material properties used in the simulation were taken from Li and Fenves (1998): density of concrete $\rho = 2643$ kg/m^3, Young's modulus $E_0 = 31027$ MPa, tensile strength $f_t = 2.9$ MPa and fracture energy $G_f = 200$ J/m^2. Note that the rate effect is approximately accounted for in this work though an increase of the tensile strength f_t by 20%, though it also can be considered as in Wu and Li (2007). Furthermore, the compressive damage is irrelevant in this example and is thus neglected. More details of the simulation are addressed elsewhere.

The numerical damage contour at the end of the simulation is shown in Figure 7. It can be clearly seen that cracks are initiated at the dam base on the upstream face due to the infinitely rigid foundation. Furthermore, cracks are also initiated at the region with stress concentration where the slope on the downstream face changes abruptly, and propagate downwards to the upstream face. The predicted damage distribution agrees fairly with the observed crack patterns reported by other investigators (Bhattacharjee and Leeger, 1993; Ghrib and Tinawi, 1995; Cervera et al., 1995; Li and Fenves, 1998).

The computed relative horizontal displacements at the left corner of the dam crest are shown in Figure 18 (the positive values represent the displacement towards downstream). It can be seen that the crest displacement remains less than 30 mm during the first 4 seconds of the earthquake, and after these 4 seconds, the amplitude of the oscillation of the crest increases substantially, implying severe damage evolution in the structure during these oscillations. Similar observation was also reported in Li and Fenves (1998) and Wu and Li (2007).

7. Concluding remarks

Aiming to the modeling of asymmetric tensile/compressive material behavior and the microcracks closure-reopening effects exhibited by concrete like quasi-brittle solids, this work addresses a novel thermodynamically consistent unilateral damage model, based on our previous work. In particular, the positive/negative projection (PNP) of the effective stress is maintained such that the conceptual simplicity and computational efficiency of the original additive bi-scalar damage constitutive relation is preserved. It is found that the classical PNP widely adopted in the literature is not optimal for this damage model, since the resulting stiffness is not always of major symmetry. Consequently, a well-defined free energy potential does not exist in general cases and the model cannot be cast into the framework of thermodynamics with internal variables. Furthermore, the damage induced anisotropy cannot be captured, exhibiting excessive lateral deformations under uniaxial tension.

In order to overcome the above issues, a novel PNP, variationally interpreted as the closest point projection of the effective stress tensor in energy norm, is proposed. Closed-form expressions of the novel PNP and the corresponding projection operators are explicitly given. With the novel PNP in energy norm, the proposed unilateral damage model always possesses stiffness tensor of major symmetry and exhibits orthotropic behavior under uniaxial tension. The corresponding thermodynamics framework is also established, resulting in an energy release rate based rounded-Rankine damage criterion appropriate for modeling tensile failure in quasi-brittle solids. Several numerical examples of single-point verifications and benchmark tests are presented. It is demonstrated that the proposed damage model is capable of characterizing tensile failure under proportional and non-proportional static loading, as well as the MCR effects under seismic cyclic loading.

Compared to our previous isotropic bi-scalar damage model (Cervera et al., 1995; Faria et al., 1998; Wu et al., 2006), the merits of the proposed one are two-fold. On the one hand, the novel PNP scheme naturally result in material stiffness tensor of major symmetry, completely restoring the thermodynamical consistency of the popular bi-scalar damage model. The ensuing symmetric secant matrix also makes it possible to use some efficient solvers, e.g., Picard's method, in solving the discrete governing equations which are in general of strong nonlinearities. On the other hand, with the novel PNP scheme the bi-scalar damage model is able to capture the orthotropic constitutive behavior at the material level. Due to the extrinsic anisotropy induced by the discretized mesh and the continuity introduced by the mixed finite element formulation or the *ad hoc* crack tracking algorithm, the significance of such an orthotropic damage model is problem dependent. In some cases, the difference of the predicted results between isotropic and anisotropic models is not pronounced, while for problems with arbitrary curved crack paths, in particular, under non-proportional loading scenarios, significant variations are observed (Fichant et al., 1999; Barbat et al., 2017).

In this work, the plastic strains are not considered, though they can be incorporated straightforwardly by the effective stress space plasticity as in Wu et al. (2006). Furthermore, it is necessary to account for the viscous (strain) rate and damping effects such that the proposed unilateral damage model can be applied to practical engineering structures. Last but not least, the proposed PNP in energy norm can also be used in the phase-field approach to fracture

(Francfort and Marigo, 1998; Bourdin et al., 2008; Miehe et al., 2010b; Wu, 2017, 2018) in which the variational minimization principle plays an important role. These topics will be addressed elsewhere.

Appendix A. Proofs of the variational inequalities

The variational inequalities (3.2) associated with the classical PNP (3.1) in Frobenius norm is similar to Proposition 1 for the novel PNP (4.1) in energy norm. As their proofs are almost the same, only the later is considered here. To this end, let us first introduce some useful lemmas (Del Piero, 1989):

Lemma 1 Two symmetric tensors, A and B are coaxial (commute) if $A \cdot B = B \cdot A$, and two coaxial symmetric tensors admit a common orthogonal basis of eigenvectors.

Lemma 2 Let $A \in \mathscr{C}$. Then

$$A : B \geq 0 \quad \forall B \in \mathscr{C}^+ (\text{or } \mathscr{C}^-) \qquad \Longrightarrow \qquad A \in \mathscr{C}^+ (\text{or } \mathscr{C}^-) \tag{A.1}$$

Moreover, if $A \in \mathscr{C}^+$, then

$$B \in \mathscr{C}^+ (\text{or } \mathscr{C}^-) \qquad \Longrightarrow \qquad A : B \geq 0 \text{ (or } \leq 0) \tag{A.2}$$

$$B \in \mathscr{C}^+ (\text{or } \mathscr{C}^-) \text{ and } A : B = 0 \qquad \Longrightarrow \qquad A \cdot B = B \cdot A = 0 \tag{A.3}$$

Proof of Proposition 1: On the one hand, assume that, for fixed $\bar{\sigma}^- \in \mathscr{C}^-$ and $\mathbb{C}_0 : \bar{\sigma}^+ \in \mathscr{C}$, Eq. $(4.2a)_1$ is verified for any $\Sigma \in \mathscr{C}^-$. Set $\Sigma = \bar{\sigma}^- + \Sigma^*$, with $\Sigma^* \in \mathscr{C}^-$. Clearly, $\Sigma \in \mathscr{C}^-$ and by Eq. $(4.2a)_1$, it follows that

$$-\Sigma^* : \mathbb{C}_0 : \bar{\sigma}^+ = \left(\bar{\sigma}^- - \Sigma\right) : \mathbb{C}_0 : \bar{\sigma}^+ \geq 0 \qquad \forall \Sigma^* \in \mathscr{C}^- \tag{A.4}$$

Hence, $\mathbb{C}_0 : \bar{\sigma}^+ \in \mathscr{C}^+$ by Eq. (A.1). Moreover, for $\Sigma^* = \bar{\sigma}^-$ we get $\bar{\sigma}^- : \mathbb{C}_0 : \bar{\sigma}^+ \leq 0$. But for $\Sigma = 0$ it follows from Eq. $(4.2a)_1$ that $\bar{\sigma}^- : \mathbb{C}_0 : \bar{\sigma}^+ \geq 0$. Therefore, $\bar{\sigma}^- : \mathbb{C}_0 : \bar{\sigma}^+ = 0$ has to hold. Conversely, if Eq. (4.1) holds, then Eq. $(4.2a)_1$ follows directly from Eq. (A.2).

On the other hand, Eq. $(4.2a)_1$ can be rewritten as

$$\bar{\sigma}^- : \mathbb{C}_0 : \bar{\sigma}^+ \geq \Sigma : \mathbb{C}_0 : \bar{\sigma}^+ \quad \forall \Sigma \in \mathscr{C}^- \tag{A.5}$$

It is exactly the argument of Eq. $(4.2a)_2$.

The alternative variational inequality (4.2b) can be similarly proved. $\square$

Appendix B. Explicit solution of the novel PNP in energy norm

Regarding the stress state, the following four cases are identified from the relation (4.5b):

(I) $\bar{\sigma}_1 \geq 0$, $\bar{\sigma}_2 \geq 0$, $\bar{\sigma}_3 \geq \nu_0(\bar{\sigma}_1 + \bar{\sigma}_2)$: The positive/negative principal values $\bar{\sigma}_n^{\pm}$ are given by

$$\begin{array}{lll} \bar{\sigma}_1^+ = \bar{\sigma}_1, & \bar{\sigma}_2^+ = \bar{\sigma}_2, & \bar{\sigma}_3^+ = \bar{\sigma}_3 \\ \bar{\sigma}_1^- = 0, & \bar{\sigma}_2^- = 0, & \bar{\sigma}_3^- = 0 \end{array} \tag{B.1a}$$

As can be seen, the pure tension state (i.e., $\bar{\boldsymbol{\sigma}}^+ = \bar{\boldsymbol{\sigma}}$ and $\bar{\boldsymbol{\sigma}}^- = \boldsymbol{0}$) for the novel projection is more restrictive than that for the classical one in which the conditions $\bar{\sigma}_n \geq 0$ suffice.

(II) $\bar{\sigma}_1 \geq 0$, $\bar{\sigma}_2 \geq 0$, $\bar{\sigma}_3 \leq \nu_0(\bar{\sigma}_1 + \bar{\sigma}_2)$: The positive/negative principal values $\bar{\sigma}_n^{\pm}$ are determined as

$$\begin{array}{lll} \bar{\sigma}_1^+ = \bar{\sigma}_1, & \bar{\sigma}_2^+ = \bar{\sigma}_2, & \bar{\sigma}_3^+ = \nu_0(\bar{\sigma}_1 + \bar{\sigma}_2) \\ \bar{\sigma}_1^- = 0, & \bar{\sigma}_2^- = 0, & \bar{\sigma}_3^- = \bar{\sigma}_3 - \nu_0(\bar{\sigma}_1 + \bar{\sigma}_2) \end{array} \tag{B.1b}$$

Note that this stress state cannot be identified from the classical projection.

(III) $\bar{\sigma}_1 \geq 0$, $\bar{\sigma}_3 \leq \bar{\sigma}_2 \leq \tilde{\nu}_0\bar{\sigma}_1$: The positive/negative principal values $\bar{\sigma}_n^{\pm}$ are solved as

$$\begin{array}{lll} \bar{\sigma}_1^+ = \bar{\sigma}_1, & \bar{\sigma}_2^+ = \tilde{\nu}_0\bar{\sigma}_1, & \bar{\sigma}_3^+ = \tilde{\nu}_0\bar{\sigma}_1 \\ \bar{\sigma}_1^- = 0, & \bar{\sigma}_2^- = \bar{\sigma}_2 - \tilde{\nu}_0\bar{\sigma}_1, & \bar{\sigma}_3^- = \bar{\sigma}_3 - \tilde{\nu}_0\bar{\sigma}_1 \end{array} \tag{B.1c}$$

for $\tilde{\nu}_0 = \nu_0/(1 - \nu_0)$. Similarly, this stress state cannot be discriminated from the classical projection.

(IV) $\bar{\sigma}_3 \leq \bar{\sigma}_2 \leq \bar{\sigma}_1 \leq 0$: This case corresponds to a pure compression state, with the following positive/negative principal values $\bar{\sigma}_n^{\pm}$

$$\begin{array}{lll} \bar{\sigma}_1^+ = 0, & \bar{\sigma}_2^+ = 0, & \bar{\sigma}_3^+ = 0 \\ \bar{\sigma}_1^- = \bar{\sigma}_1, & \bar{\sigma}_2^- = \bar{\sigma}_2, & \bar{\sigma}_3^- = \bar{\sigma}_3 \end{array} \tag{B.1d}$$

This pure compression state with $\bar{\boldsymbol{\sigma}}^+ = \boldsymbol{0}$ and $\bar{\boldsymbol{\sigma}}^- = \bar{\boldsymbol{\sigma}}$ coincides with that of the classical projection.

Note that the continuity between different stress states is guaranteed. Furthermore, the above results for cases (I), (II) and (IV) apply to the plane stress condition ($\bar{\sigma}_2 = 0$), with the out-of-plane stress $\bar{\sigma}_2$ neglected.

Appendix C. Stiffness and compliance matrices in the principal space

Let us now verify the major symmetry of the secant stiffness (2.9b) and compliance (2.13a) with the novel PNP in energy norm. Only the secant compliance is addressed here since the expressions are much simpler, while the stiffness is obtained straightforwardly from the matrix inverse. Furthermore, it is sufficient to consider only the compliance matrix in the space of principal effective stresses.

In the space of principal effective stresses, the linear elastic relation (2.1) relates the principal strains ϵ_n to the principal effective stresses $\bar{\sigma}_n$, where the later $\bar{\sigma}_n$ can be expressed in terms of the nominal counterparts σ_n by calling

for the additive bi-scalar damage constitutive relation (2.10) and the positive/negative components $\bar{\sigma}_n^\pm$ explicitly given above. Accordingly, the secant compliance matrix $[\mathbb{C}]$ can be derived, together with the damage tensor $\mathbb{D} = \mathbb{I} - \mathbb{C}^{-1} : \mathbb{C}_0$ in matrix form.

Regarding the stress state, the following four cases are identified:

(I) $\bar{\sigma}_1 \geq 0$, $\bar{\sigma}_2 \geq 0$, $\bar{\sigma}_3 \geq \nu_0(\bar{\sigma}_1 + \bar{\sigma}_2)$: In this case, Eqs. (2.10) and (B.1a) give the following principal stresses

$$\sigma_n = (1 - d^+)\bar{\sigma}_n \tag{C.1}$$

such that

$$[\mathbb{C}] = \frac{1}{(1-d^+)E_0}\begin{bmatrix} 1 & -\nu_0 & -\nu_0 \\ -\nu_0 & 1 & -\nu_0 \\ -\nu_0 & -\nu_0 & 1 \end{bmatrix}, \qquad [\mathbb{D}] = d^+\begin{bmatrix} 1 & 0 & 0 \\ 0 & 1 & 0 \\ 0 & 0 & 1 \end{bmatrix} \tag{C.2}$$

As expected, the pure tension results in an isotropic damage state.

(II) $\bar{\sigma}_1 \geq 0$, $\bar{\sigma}_2 \geq 0$, $\bar{\sigma}_3 \leq \nu_0(\bar{\sigma}_1 + \bar{\sigma}_2)$: Eqs. (2.10) and (B.1b) yield

$$\sigma_1 = (1 - d^+)\bar{\sigma}_1, \qquad \sigma_2 = (1 - d^+)\bar{\sigma}_2, \qquad \sigma_3 = (1 - d^-)\bar{\sigma}_3 - \tilde{d}\nu_0(\bar{\sigma}_1 + \bar{\sigma}_2) \tag{C.3}$$

for the difference $\tilde{d} := d^+ - d^-$ between the tensile and compressive damage variables. The corresponding secant stiffness matrix $[\mathbb{C}]$ and damage matrix $[\mathbb{D}]$ are determined as

$$[\mathbb{C}] = \frac{1}{(1-d^-)E_0}\begin{bmatrix} \dfrac{(1-d^-) - \tilde{d}\nu_0^2}{1-d^+} & -\dfrac{(1-d^-) + \tilde{d}\nu_0}{1-d^+}\nu_0 & -\nu_0 \\ -\dfrac{(1-d^-) + \tilde{d}\nu_0}{1-d^+}\nu_0 & \dfrac{(1-d^-) - \tilde{d}\nu_0^2}{1-d^+} & -\nu_0 \\ -\nu_0 & -\nu_0 & 1 \end{bmatrix} \tag{C.4}$$

$$[\mathbb{D}] = \begin{bmatrix} d^+ & 0 & 0 \\ 0 & d^+ & 0 \\ \nu_0\tilde{d} & \nu_0\tilde{d} & d^- \end{bmatrix} \tag{C.5}$$

Accordingly, the resulting damage model is an orthotropic one. Furthermore, due to the non-vanishing Poisson's ratio the compressive damage d^- affects the lateral tensile behavior.

(III) $\bar{\sigma}_1 \geq 0$, $\bar{\sigma}_3 \leq \bar{\sigma}_2 \leq \tilde{\nu}_0\bar{\sigma}_1$: It then follows from Eqs. (2.10) and (B.1c) that

$$\sigma_1 = (1 - d^+)\bar{\sigma}_1, \qquad \sigma_2 = (1 - d^-)\bar{\sigma}_2 - \tilde{d}\tilde{\nu}_0\bar{\sigma}_1, \qquad \sigma_3 = (1 - d^-)\bar{\sigma}_3 - \tilde{d}\tilde{\nu}_0\bar{\sigma}_1 \tag{C.6a}$$

leading to

$$[\mathbb{C}] = \frac{1}{(1-d^-)E_0}\begin{bmatrix} \dfrac{(1-d^-) - 2\tilde{d}\tilde{\nu}_0\nu_0}{1-d^+} & -\nu_0 & -\nu_0 \\ -\nu_0 & 1 & -\nu_0 \\ -\nu_0 & -\nu_0 & 1 \end{bmatrix} \tag{C.7}$$

$$
\left[\mathbb{D}\right] = \begin{bmatrix} d^+ & 0 & 0 \\ \tilde{v}_0\tilde{d} & d^- & 0 \\ \tilde{v}_0\tilde{d} & 0 & d^- \end{bmatrix} \tag{C.8}
$$

Similarly to Case (II), the tensile behavior is also affected by the lateral compressive damage d^-.

(IV) $\bar{\sigma}_3 \leq \bar{\sigma}_2 \leq \bar{\sigma}_1 \leq 0$: In this case, Eqs. (2.10) and (B.1d) give

$$
\sigma_n = \left(1 - d^-\right)\bar{\sigma}_n \tag{C.9}
$$

such that

$$
\left[\mathbb{C}\right] = \frac{1}{\left(1 - d^-\right)E_0} \begin{bmatrix} 1 & -v_0 & -v_0 \\ -v_0 & 1 & -v_0 \\ -v_0 & -v_0 & 1 \end{bmatrix}, \qquad \left[\mathbb{D}\right] = d^- \begin{bmatrix} 1 & 0 & 0 \\ 0 & 1 & 0 \\ 0 & 0 & 1 \end{bmatrix} \tag{C.10}
$$

As can be seen, an isotropic damage model is recovered under the pure compression.

With the out-of-plane stress $\bar{\sigma}_2$ neglected, the above results for cases (I), (II) and (IV) apply to the plane stress condition ($\bar{\sigma}_2 = 0$). In all cases, the compliance matrix $[\mathbb{C}]$ is symmetric, guaranteeing the major symmetry of the secant stiffness tensor $\mathbb{E}$.

References

Abu Al-Rub, R., Kim, S., 2010. Computational applications of a coupled plasticity-damage constitutive model for simulating plain concrete fracture. Engineering Fracture Mechanics 77 (10), 1577–1603.

Alfano, G., Rosati, L., Valoroso, N., 2000. A numerical strategy for finite element analysis of no-tension materials. Int. J. Numer. Meth. Engng. 48, 317–350.

Arrea, M., Ingraffea, A., 1982. Mixed-mode crack propagation in mortar and concrete. Tech. Rep. Report No. 81-13, Department of Structural Engineering, Cornell University, Ithaca, NY.

Barbat, G. B., Cervera, M., Chiumenti, M., 2017. Appraisement of planar, bending and twisting cracks in 3d with isotropic and orthotropic damage models. International Journal of Fracture http://dx.doi.org/10.1007/s10704-018-0261-3.

Bažant, Z. P., Oh, B. H., 1983. Crack band theory for fracture of concrete. Mater. Struct. 16, 155–177.

Bhattacharjee, S., Leeger, P., 1993. Seismic cracking and energy dissipation in concrete gravity dams. Earthq. Eng. Struct. Dyn. 22, 991–1007.

Bourdin, B., Francfort, G., Marigo, J.-J., 2008. The variational approach to fracture. Springer, Berlin.

Carol, I., Rizzi, E., Willam, K., 2001. On the formulation of anisotropic elastic degradation. i. theory based on a pseudo-logarithmic damage tensor rate. Int. J. Solids Structures 38, 491–518.

Carol, I., Willam, K., 1996. Spurious energies dissipation/generation in stiffness recovery models for elastic degradation and damage. Int. J. Solids Structures 33 (20-22), 2939–2957.

Cendón, D., Gálvez, J., Elices, M., Planas, J., 2000. Modeling the fracture of concrete under mixed loading. International Journal of Fracture 103, 293–210.

Cervera, M., Agelet de Saracibar, C., Chiumenti, M., 2002. Comet: Coupled mechanical and thermal analysis. data input manual, version 5.0. Tech. Rep. Technical Report IT-308, CIMNE, Technical University of Catalonia, Available from: http://www.cimne.upc.es.

Cervera, M., Barbat, G., Chiumenti, M., 2017. Finite element modeling of quasi-brittle cracks in 2d and 3d with enhanced strain accuracy. Comput. Mech. 60 (5), 767796.

Cervera, M., Chiumenti, M., Codina, R., 2010a. Mixed stabilized finite element methods in nonlinear solid mechanics. part i: Formulation. Computer Methods in Applied Mechanics and Engineering 199 (37-40), 2559–2570.

Cervera, M., Chiumenti, M., Codina, R., 2010b. Mixed stabilized finite element methods in nonlinear solid mechanics. part ii: Strain localization. Computer Methods in Applied Mechanics and Engineering 199 (37-40), 2571–2589.

Cervera, M., Chiumenti, M., Codina, R., 2011. Mesh objective modeling of cracks using continuous linear strain and displacement interpolations. Int. J. Numer. Meth. Engng. 87 (10), 962–987.

Cervera, M., Oliver, J., Faria, R., 1995. Seismic evaluation of concrete dams via continuum damage models. Earthq. Eng. Struct. Dyn. 24, 1225–1245.

Cervera, M., Pelà, L., Clemente, R., Roca, P., 2010c. A crack-tracking technique for localized damage in quasi-brittle materials. Engineering Fracture Mechanics 77, 2431–2450.

Cervera, M., Tesei, C., 2017. An energy-equivalent d+/d- damage model with enhanced microcrack closure-reopening capabilities for cohesive-frictional materials. Materials 10 (4), 433, doi: 10.3390/ma10040433.

CIMNE, 2009. Gid: The personal pre and post processor Available from: http://www.gidhome.com.

Coleman, B., Gurtin, M., 1967. Thermodynamics with internal state variables. Journal of Chemistry and Physics 47, 597–613.

Comi, C., Perego, U., 2001. Fracture energy based bi-dissipative damage model for concrete. Int. J. Solids Structures 38, 6427–6454.

Cordebois, J., Sidoroff, F., 1982. Endommagement anisotrope en elasticit et plasticit. J. Mec. Theor. Appl. Special volume (2), 45–60.

de Borst, R., 1987. Computation of post-bifurcation and post-failure behavior of strain-softening solids. Computers and Structures 25, 211–224.

Del Piero, G., 1989. Constitutive equation and compatibility of the external loads for linear elastic masonry-like materials. Meccanica 24, 150–162.

Faria, R., Oliver, J., Cervera, M., 1998. A strain-based plastic viscous-damage model for massive concrete structures. International Journal of Solids Structures 35 (14), 1533–1558.

Faria, R., Oliver, J., Cervera, M., 2000. On isotropic scalar damage models for the numerical analysis of concrete structures. CIMNE Monograph, No. 198, Barcelona, Spain.

Fichant, S., La Borderie, C., Pijaudier-Cabot, G., 1999. Isotropic and anisotropic descriptions of damage in concrete structures. Mech. Cohes.-Frict. Mater. 4, 339–359.

Francfort, G., Marigo, J., 1998. Revisting brittle fracture as an energy minimization problem. J. Mech. Phys. Solids 46 (8), 1319–1342.

Freddi, F., Royer-Carfagni, G., 2010. Regularized variational theories of fracture: A unified approach. J. Mech. Phys. Solids 58, 1154–1174.

Gálvez, J., Elices, M., Guinea, G., Planas, J., 1998. Mixed mode fracture of concrete under proportional and nonproportional loading. Int. J. Fract. 94, 267–284.

Gálvez, J., Elices, M., Guinea, G., Planas, J., 2000. Modelling the fracture of concrete under mixed loading. Int. J. Fract. 103, 293–310.

Gernay, T., Millard, A., Franssen, J.-M., 2013. A multiaxial constitutive model for concrete in the fire situation: Theoretical formulation. Int. J. Solids Structures 50, 3659–3673.

Ghrib, F., Tinawi, R., 1995. An application of damage mechanics for seismic analysis of concrete gravity dams. Earthq. Eng. Struct. Dyn. 24, 157–173.

Grassl, P., Xenos, D., Nyström, U., Rempling, R., Gylltoft, K., 2013. Cdpm2: A damage-plasticity approach to modelling the failure of concrete. Int. J. Solids Structures 50, 3805–3816.

Hansen, N., Schreyer, H., 1994. A thermodynamically consistent framework for theories of elastoplasticity coupled with damage. Int. J. Solids Struct. 31 (3), 359–389.

Hansen, N., Schreyer, H., 1995. Damage deactivation. J. Appl. Mech., ASME 62, 450–458.

Hilber, H., Hughes, T., Talor, R., 1977. Improved numerical dissipation for time integration algorithms in structural dynamics. Earthquake Engineering and Structural Dynamics 5, 282–292.

Ju, J., 1989. On energy-based coupled elastoplastic damage theories: constitutive modeling and computational aspects. Int. J. Solids Structures 25 (7), 803–833.

Ju, J., 1990. Isotropic and anisotropic damage variables in continuum damage mechanics. Journal of Engineering Mechanics, ASCE 116 (12), 2764–2770.

Kachanov, L., 1958. Time rupture process under creep conditions. Izv. A Rad. Nauk. SSSR otd Tekh. Nauk 8, 26–31.

Krajcinovic, D., 2003. Damage Mechanics. Elsevier B.V., the Netherlands.

Lemaitre, J., Desmorat, R., 2005. Engineering Damage Mechanics. Spring-Verlag, Berlin.

Li, J., Fenves, G., 1998. A plastic-damage concrete model for earthquake analysis of dams. Earthquake Engng. Struct. Dyn. 27, 937–956.

Li, J., Ren, X., 2009. Stochastic damage model for concrete based on energy equivalent strain. Int. J. Solids Structures 46, 2407–2419.

Li, T., Marigo, J.-J., Guilbaud, D., Potapov, S., 2016. Gradient damage modeling of brittle fracture in an explicit dynamics context. Int. J. Numer. Meth. Engng. 108 (11), 1381–1405.

Lubarda, V., Krajcinovic, D., Mastilovic, S., 1994. Damage model for brittle elastic solids with unequal tensile and compressive strengths. Eng. Fract. Mech. 49, 681697.

Mahnken, R., Tikhomirov, D., Stein, E., 2000. Implicit integration scheme and its consistent linearization for an elastoplastic-damage model with application to concrete. Computers and Structures 75, 135–143.

Mazars, J., Berthaud, Y., Ramtani, S., 1990. The unilateral behavior of damaged concrete. Eng. Frac. Mech. 35, 629–635.

Mazars, J., Pijaudier-Cabot, G., 1989. Continuum damage theory: application to concrete. Journal of Engineering Mechanics, ASCE 115 (2), 345–365.

Meyer, C. D., 2000. Matrix Analysis and Applied Linear Algebra. Society for Industrial and Applied Mathematics.

Miehe, C., Hofacker, M., Welschinger, F., 2010a. A phase field model for rate-independent crack propagation: Robust algorithmic implementation based on operator splits. Computer Methods in Applied Mechanics and Engineering 199 (45-48), 2765 – 2778.

Miehe, C., Welschinger, F., Hofacker, M., 2010b. Thermodynamically consistent phase-field models of fracture: Variational principles and multi-field fe implementations. Int. J. Numer. Meth. Engng. 83, 1273–1311.

Moreau, J., 1974. On unilateral constraints, friction and plasticity. In: New variational techniques in Mathematical Physics. CIME Course, Springer-Verlag, 1974.

Murakami, S., 2012. Continuum Damage Mechanics. Springer, New York.

Nguyen, Q. S., 2000. Stability and nonlinear solid mechanics. John Wiley & Sons, Ltd., Singapore.

Ortiz, M., 1985. A constitutive theory for inelastic behaviour of concrete. Mech. Mater. 4, 67–93.

Ožbolt, J., Li, Y., Kožar, I., 2001. Microplane model for concrete with relaxed kinematic constraint. Int. J. Solids Struct. 38, 2683–2711.

Peerlings, R., de Borst, R., Brekelmans, W., de Vree, J., 1996. Gradient-enhanced damage for quasi-brittle materials. Int. J. Numer. Methods Engng. 39, 3391–3403.

Pelà, L., Cervera, M., Roca, P., 2011. Continuum damage model for orthotropic materials: Application to masonry. Computer Methods and Applied Mechanics in Engineering 200 (9-12), 917–930.

Pijaudier-Cabot, G., Bažant, Z., 1987. Nonlocal damage theory. J. Engng. Mech., ASCE 113, 1512–1533.

Reinhardt, H., Cornelissen, H., 1984. Postpeak cyclic behavior of concrete in uniaxial tensile and alternating tensile and compressive loading. Cem. Concr. Res. 14, 263–270.

Rots, J., 1988. Computational modeling of concrete fracture. Ph.D. thesis, Delft University of Technology, the Netherlands.

Rots, J., Nauta, P., Kusters, G., Blaauwendraad, J., 1985. Smeared crack approach and fracture localization in concrete. Heron 30, 1–47.

Simó, J., Hughes, T., 1998. Computational inelasticity. Springer, New York.

Simó, J., Ju, J., 1987. Strain- and stress-based continuum damage models. i: Formulation; ii: Computational aspects. Int. J. Solids Structure 23 (7), 821–869.

Westergaard, H., 1933. Water pressures on dams during earthquakes. Transactions of the American Society of Civil Engineers 98, 418–433.

Wu, J. Y., 2017. A unified phase-field theory for the mechanics of damage and quasi-brittle failure in solids. Journal of the Mechanics and Physics of Solids 103, 72–99.

Wu, J. Y., 2018. A geometrically regularized gradient-damage model with energetic equivalence. Comput. Methods Appl. Mech. Engrg. 328, 612–637.

Wu, J. Y., Cervera, M., 2017. Strain localization of elastic-damaging frictional-cohesive materials: Analytical results and numerical verification. Materials 10, 434; doi:10.3390/ma10040434.

Wu, J. Y., Li, J., 2007. Unified plastic-damage model for concrete and its applications to dynamic nonlinear analysis of structures. Structural Engineering and Mechanics 25 (5), 519–540.

Wu, J. Y., Li, J., Faria, R., 2006. An energy release rate-based plastic-damage model for concrete. International Journal of Solids and Structures 43, 583–612.

Wu, J. Y., Xu, S. L., 2011. An augmented multicrack elastoplastic damage model for tensile cracking. International Journal of Solids and Structures 48, 2511–2528.

Wu, J. Y., Xu, S. L., 2013. Reconsideration on the elastic damage/degradation theory for the modeling of microcrack closure-reopening (mcr) effects. International Journal of Solids and Structures 50, 795–805.

Yazdani, S., Schreyer, H., 1990. Combined plasticity and damage mechanics model for plain concrete. J. Eng. Mech. ASCE 116, 1435–1450.
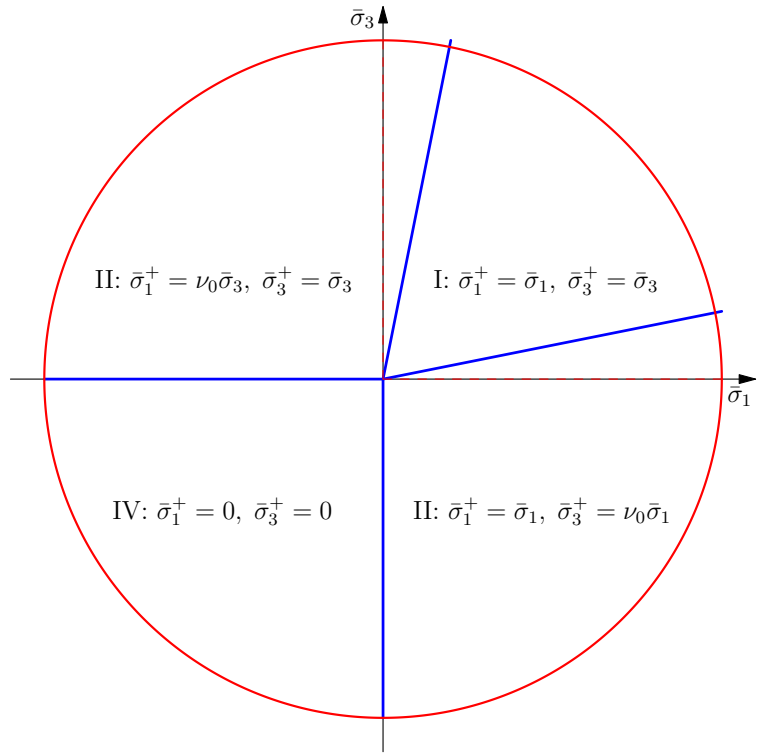
Figure 1: Positive principal effective stresses of the novel PNP in the 2-D plane stress condition

In Figure 1:

II: $\bar{\sigma}_1^+ = \nu_0 \bar{\sigma}_3$, $\bar{\sigma}_3^+ = \bar{\sigma}_3$

I: $\bar{\sigma}_1^+ = \bar{\sigma}_1$, $\bar{\sigma}_3^+ = \bar{\sigma}_3$

IV: $\bar{\sigma}_1^+ = 0$, $\bar{\sigma}_3^+ = 0$

II: $\bar{\sigma}_1^+ = \bar{\sigma}_1$, $\bar{\sigma}_3^+ = \nu_0 \bar{\sigma}_1$
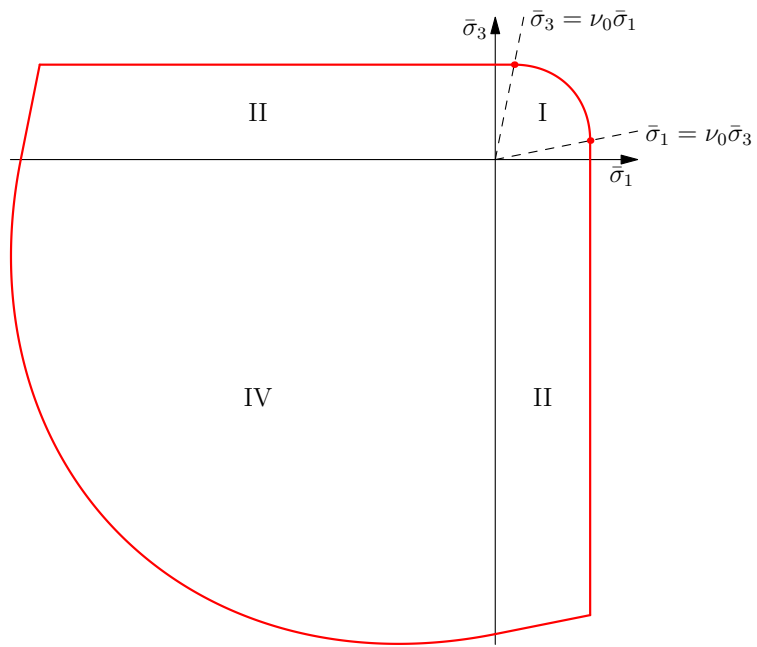
Figure 2: Elastic domain in the 2-D plane stress condition

In Figure 2:

$\bar{\sigma}_3 = \nu_0 \bar{\sigma}_1$

$\bar{\sigma}_1 = \nu_0 \bar{\sigma}_3$

31
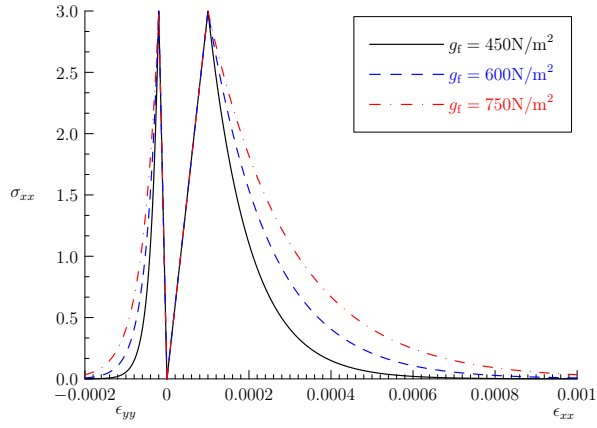
(a) Axial and lateral responses given by the classical PNP scheme
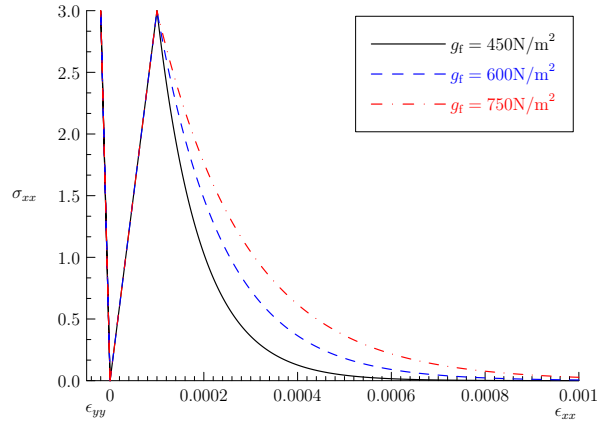
(b) Axial and lateral responses given by the novel PNP scheme

Figure 3: Numerical results under uniaxial tension for various specific fracture energy g_{f}: Axial stress σ_{xx} *versus* axial strain ϵ_{xx} and lateral strain ϵ_{yy}
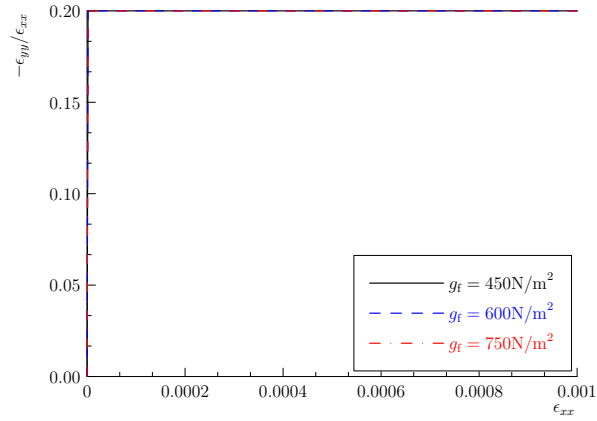
(a) Nominal Poisson's ratio given by the classical PNP scheme
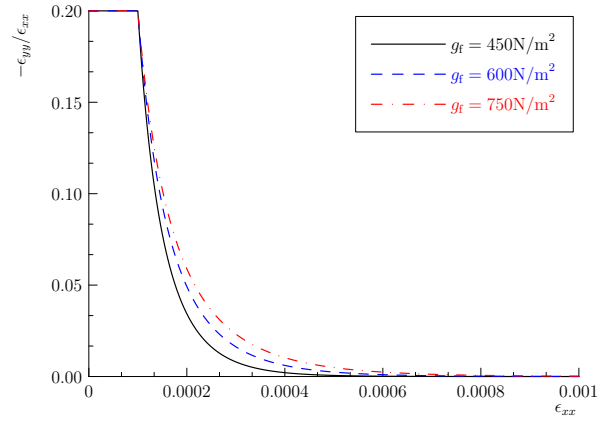
(b) Nominal Poisson's ratio given by the novel PNP scheme

Figure 4: Numerical results under uniaxial tension for various specific fracture energy g_{f}: Nomial Poisson's ratio $-\epsilon_{yy}/\epsilon_{xx}$ *versus* axial strain ϵ_{xx}

(a) Normal stress σ_{xx} *versus* shear strain ϵ_{xy}

(b) Shear stress σ_{xy} *versus* shear strain ϵ_{xy}

(c) Principle stress σ_1 *versus* principle strain ϵ_1

(d) Principle stress σ_3 *versus* principle strain ϵ_3
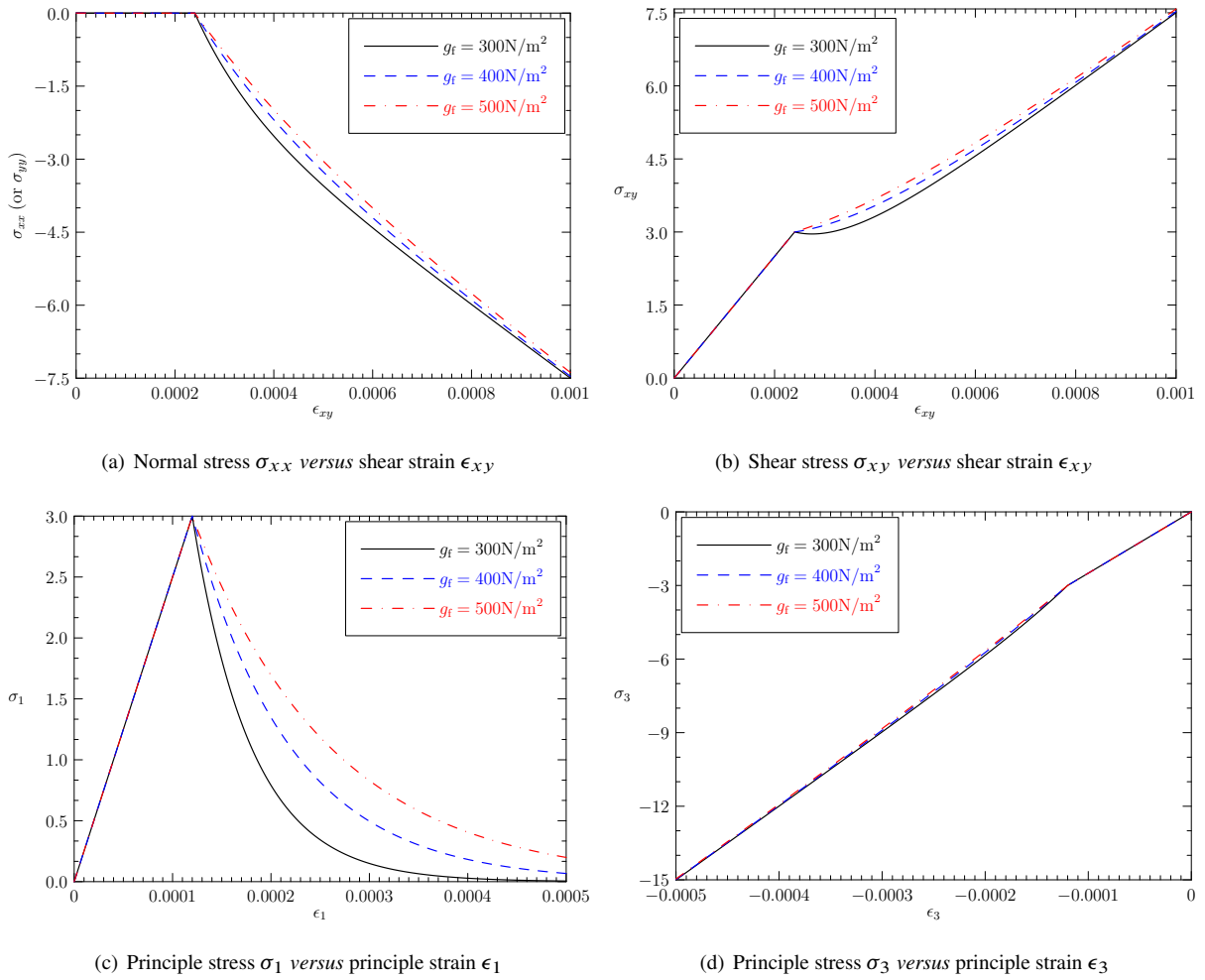
Figure 5: Numerical results of pure torsion for various specific fracture energy g_f

(a) Load path of the cyclic tension and compression

(b) Axial stress σ_{xx} *versus* axial strain ϵ_{xx}
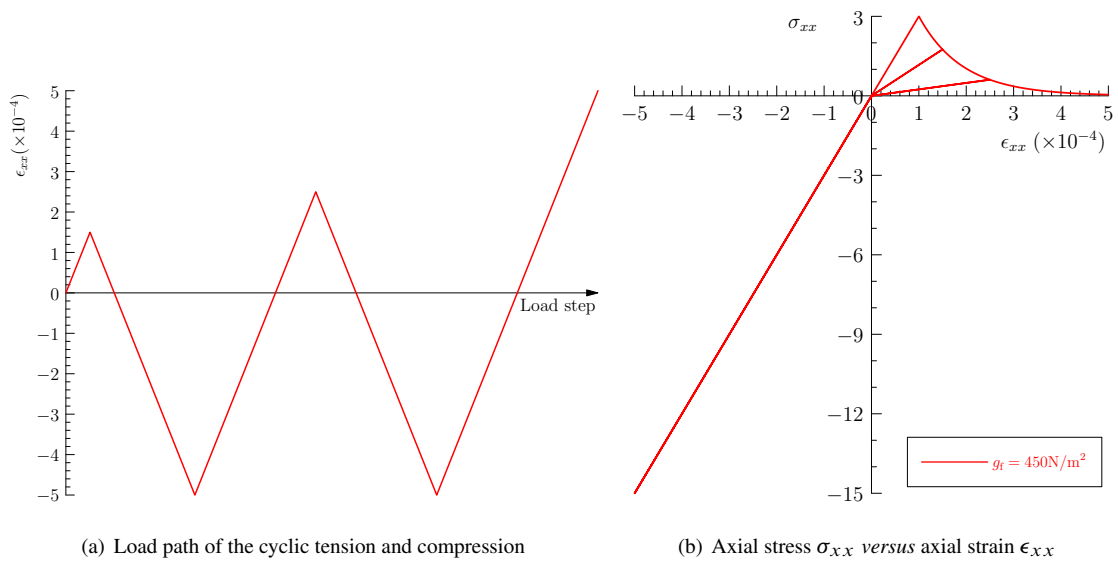
Figure 6: Numerical predictions of cyclic uniaxial tension/compression (the compressive damage is neglected temporarily)

33

(a) Geometry   (b) Finite element mesh   (c) Zoomed finite element mesh
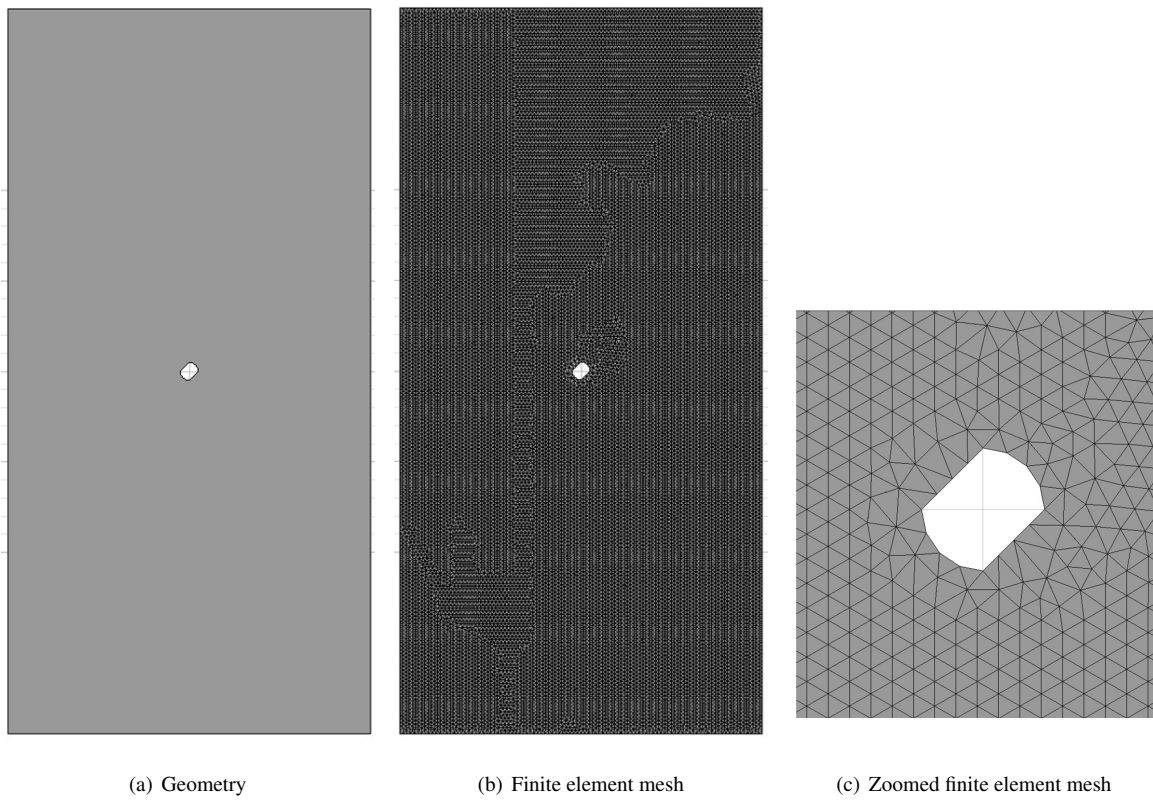
Figure 7: Uniaxial stretch of a perforated strip: Problem setting

(a) Displacement u_y ($\nu_0 = 0.0$)   (b) Damage d^+ ($\nu_0 = 0.0$)   (c) Displacement u_y ($\nu_0 = 0.3$)   (d) Damage d^+ ($\nu_0 = 0.3$)
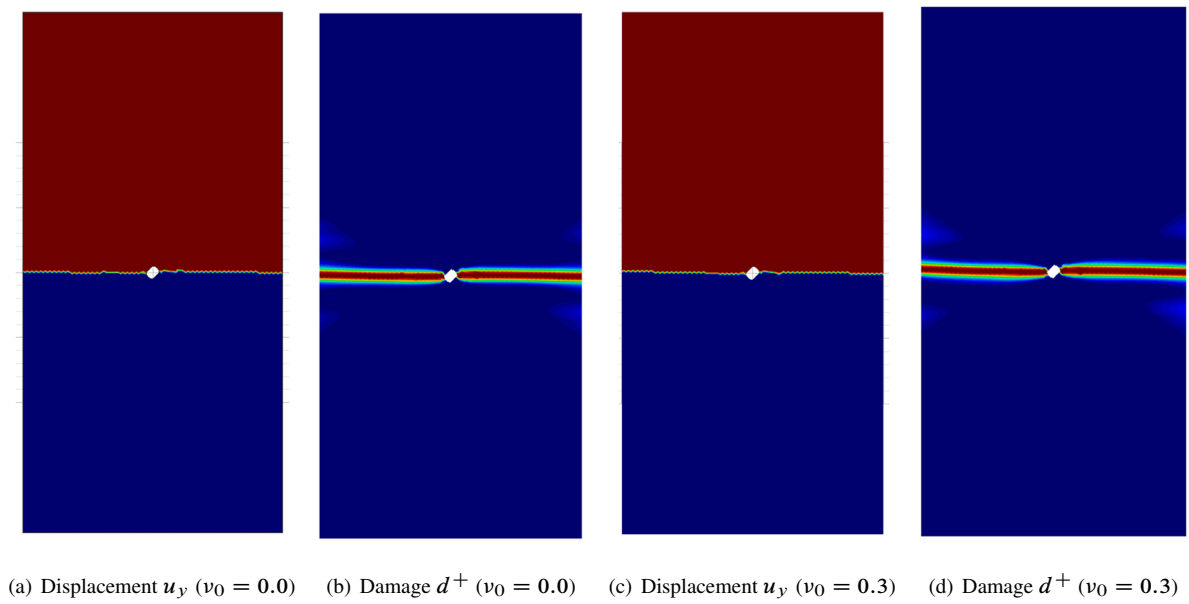
Figure 8: Uniaxial stretch of a perforated strip: contours of vertical displacements and damage for various Poisson's ratios

34
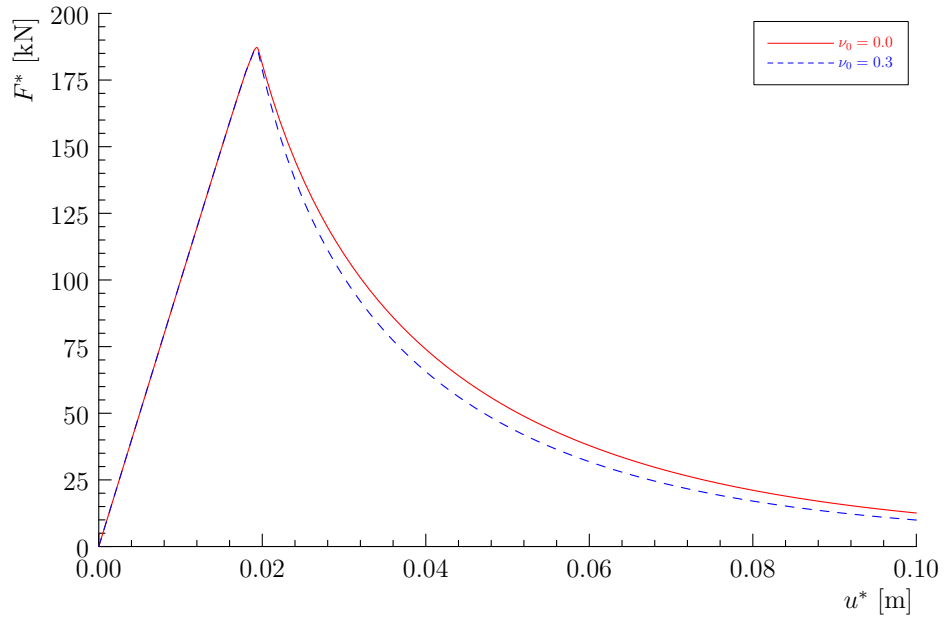
(a) Various Poisson's ratios
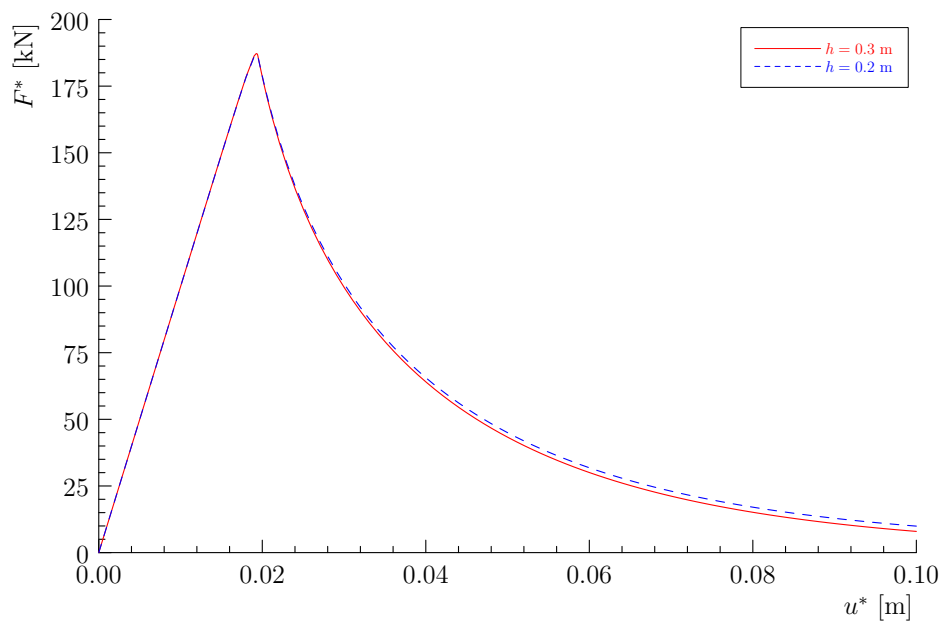
(b) Various mesh sizes

Figure 9: Uniaxial stretch of a perforated strip: Applied load *versus* vertical displacement for various Poisson's ratios and mesh sizes
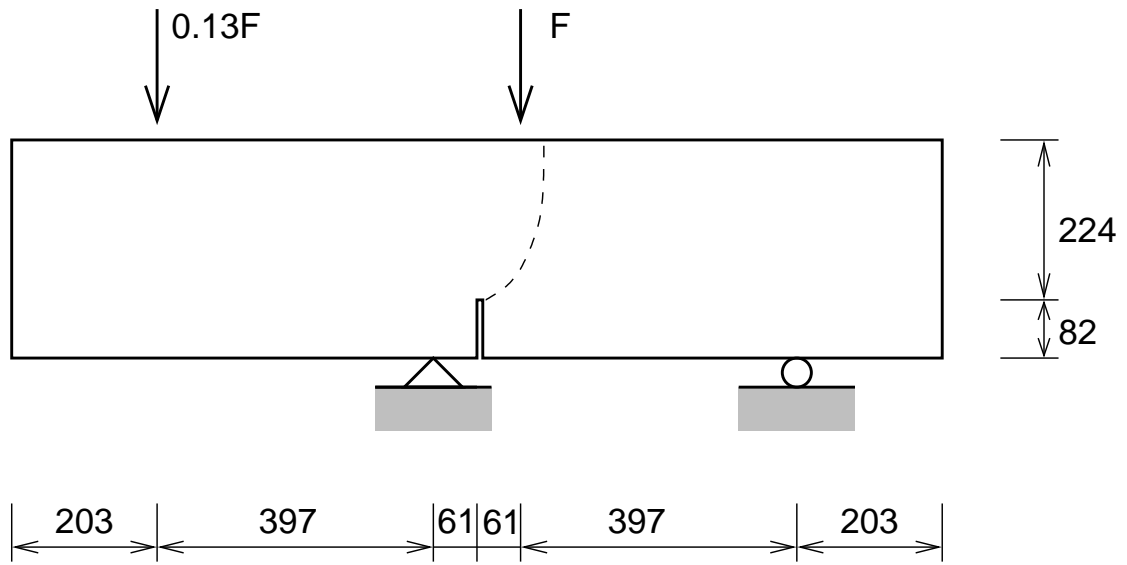
(a) Geometry (unit: mm), boundary and loading conditions
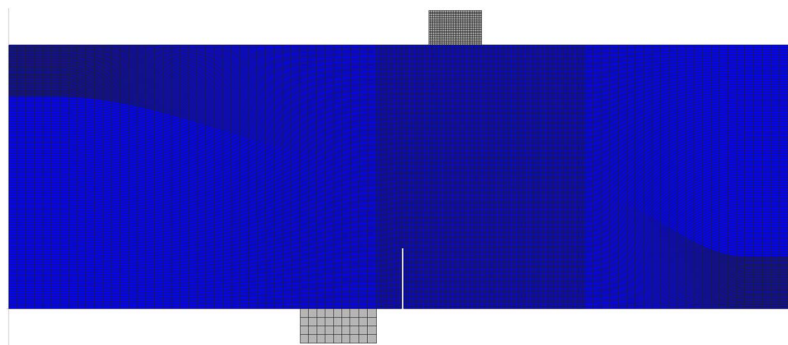
(b) Finite element mesh
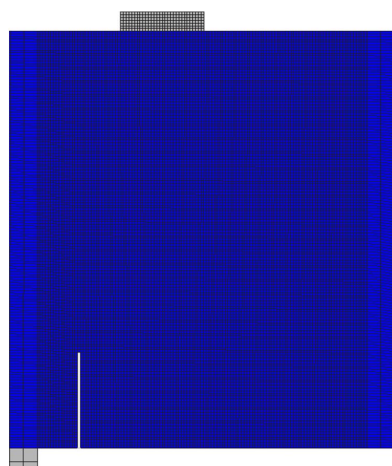
(c) Finite element mesh zoomed around the notch

Figure 10: Single edge-notched beams under proportional loading (Arrea and Ingraffea, 1982): Problem setting
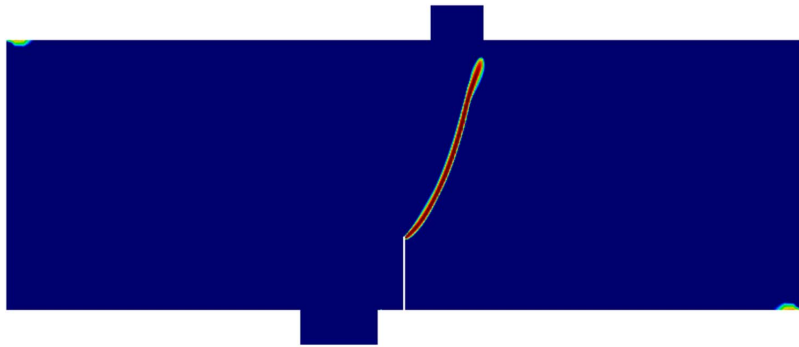
Figure 11: Single edge-notched beams under proportional loading (Arrea and Ingraffea, 1982): Damage contours
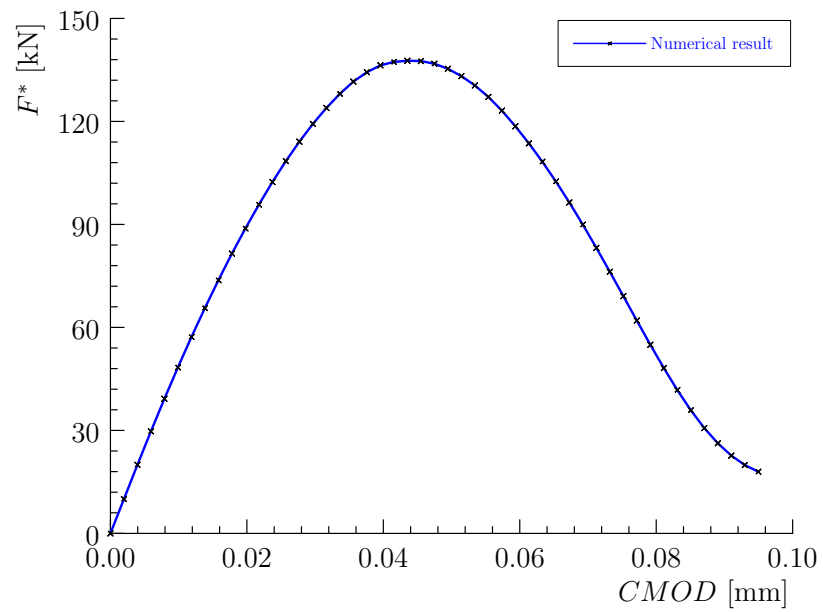
Figure 12: Single edge-notched beam under proportional loading (Arrea and Ingraffea, 1982): Load *versus* CMSD curves for series A and C
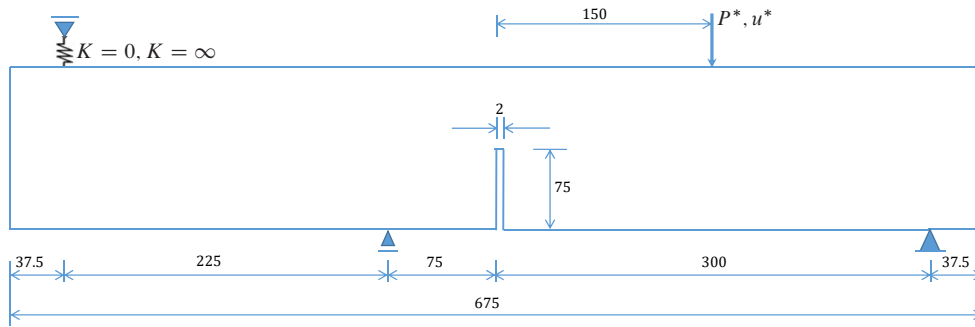
(a) Geometry (unit: mm), boundary and loading conditions
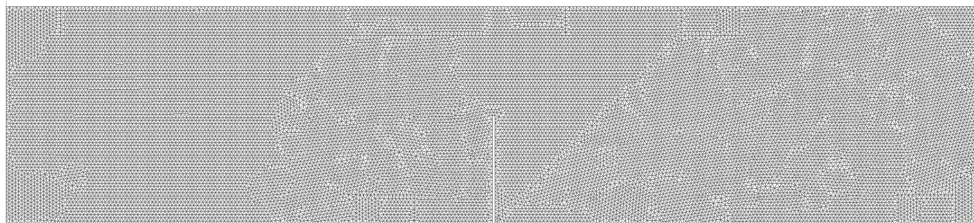
(b) Finite element mesh
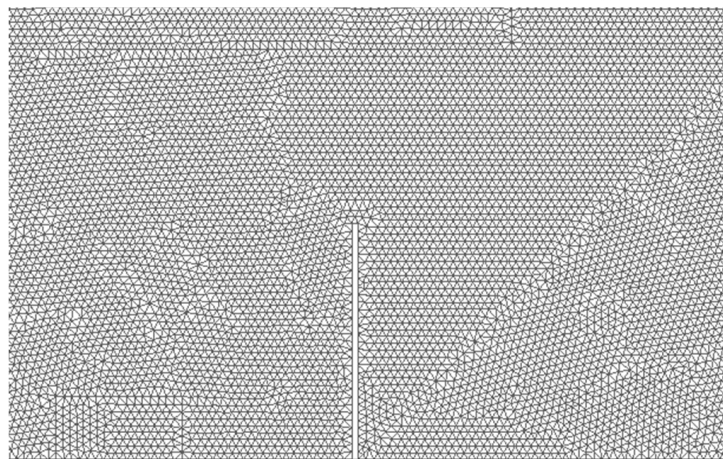
(c) Finite element mesh zoomed around the notch

Figure 13: Three- and four-point bending single edge-notched beam under non-proportional loading (Gálvez et al., 1998): Problem setting
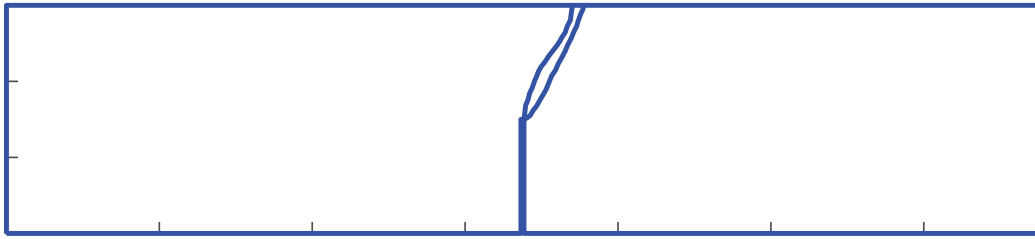
(a) Experimentally observed crack paths
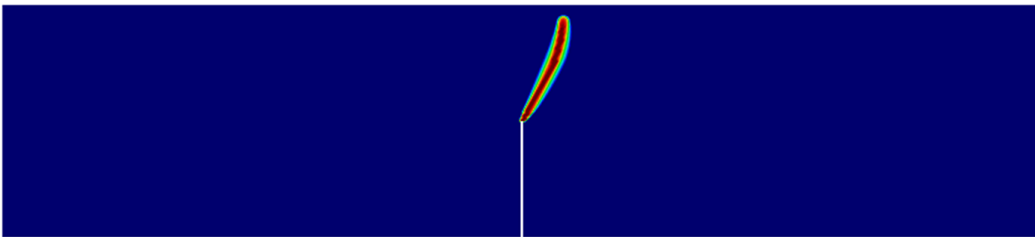
(b) Numerically obtained damage contour

Figure 14: Three-point bending single edge-notched beam: Comparison between the experimentally observed crack paths (Gálvez et al., 1998) and the numerically obtained damage contour
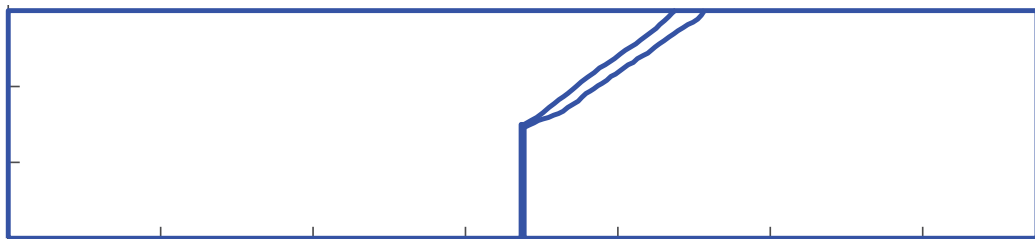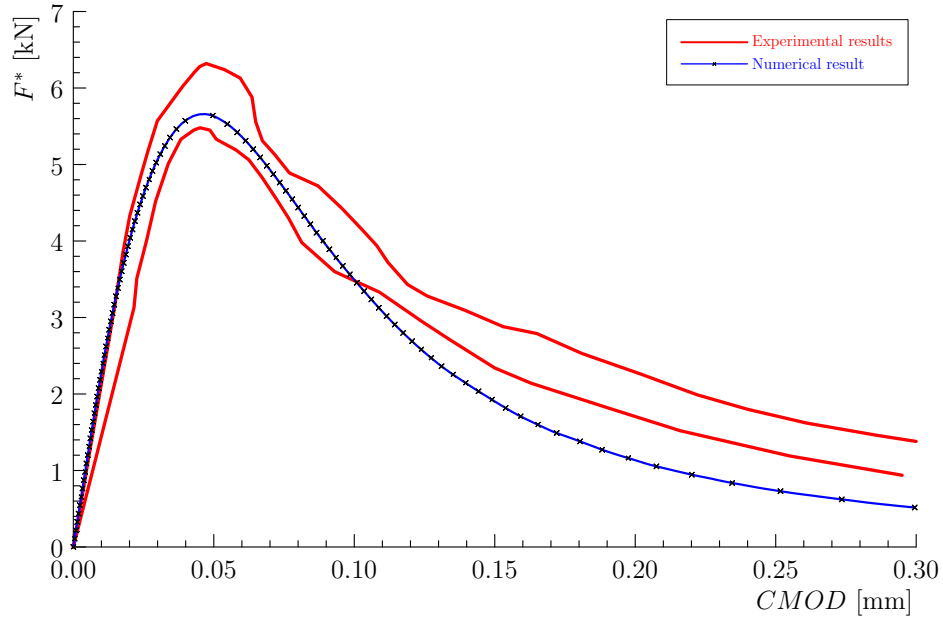

(a) Experimentally observed crack paths
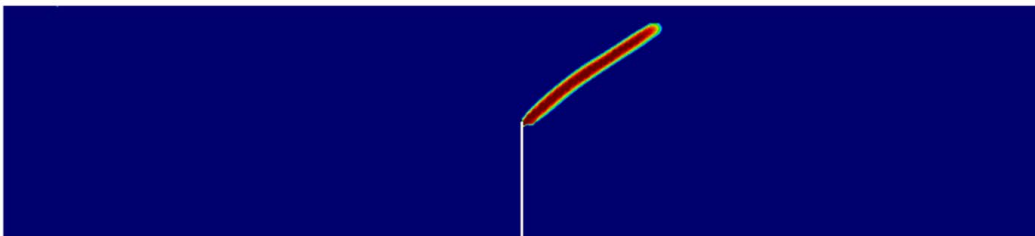
(b) Numerically obtained damage contour

Figure 15: Four-point bending single edge-notched beam: Comparison between the experimentally observed crack paths (Gálvez et al., 1998) and the numerically obtained damage contour

Figure 16: Three-point bending single edge-notched beam (Gálvez et al., 1998): Load *versus* CMOD curves
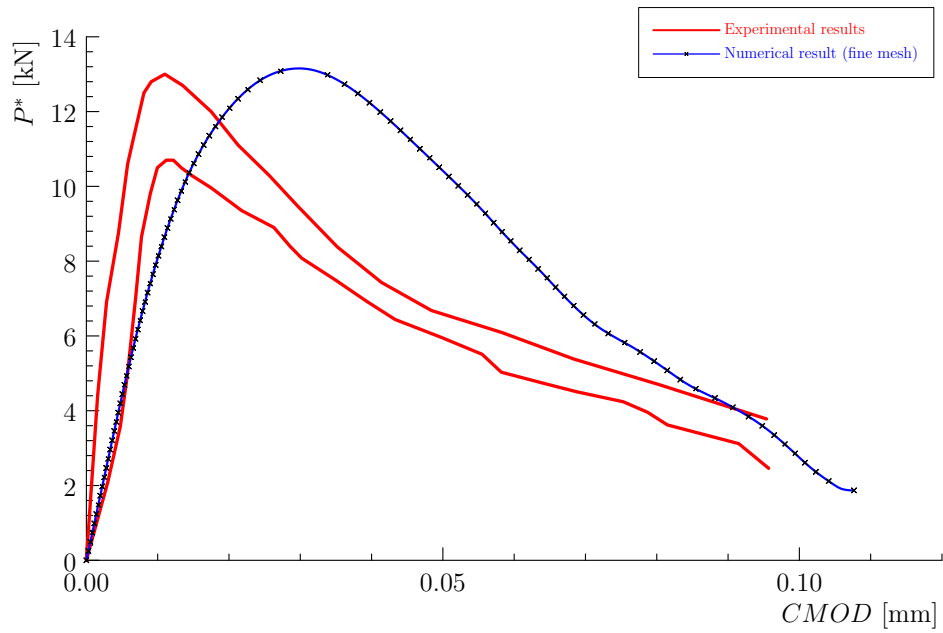

Figure 17: Four-point bending single edge-notched beam (Gálvez et al., 1998): Load *versus* CMOD curves
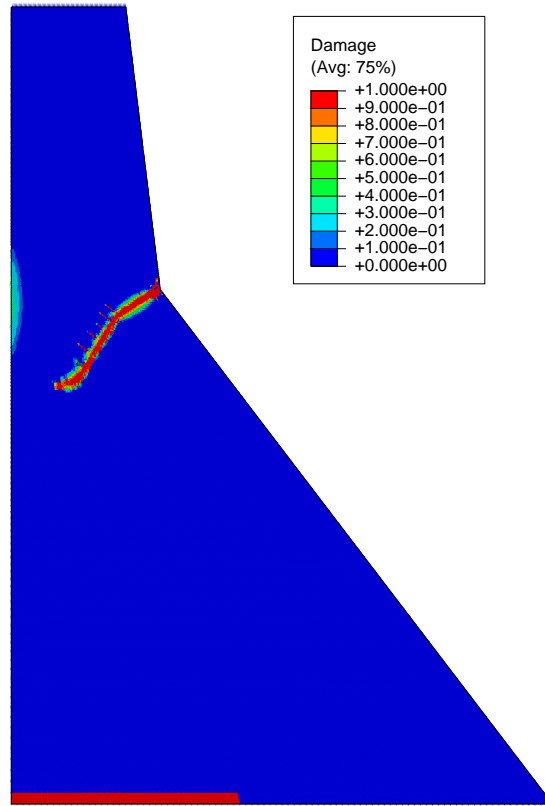
Figure 18: Koyna dam: Damage contour at the end of the simulation with dam-reservoir hydrodynamic interactions
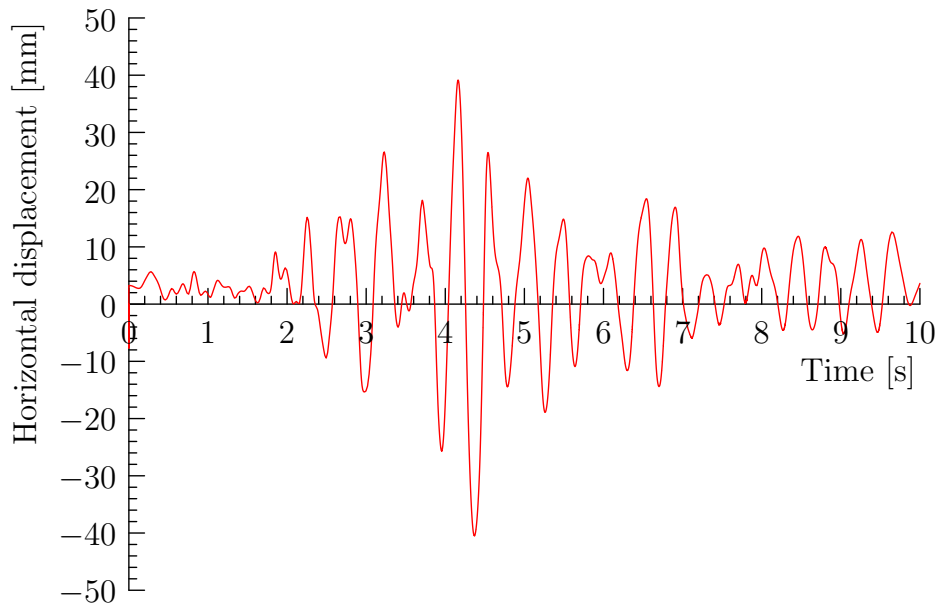

Figure 19: Koyna dam: Horizontal crest displacement (relative to the ground displacements)

41